Solid Earth forcing of Mesozoic oceanic anoxic events

T. M. Gernon ●[1] ✉, B. J. W. Mills ●[2], T. K. Hincks ●[1], A. S. Merdith ●[2,3], L. J. Alcott ●[4,5,6,8], E. J. Rohling[1,7] & M. R. Palmer ●[1]

Oceanic anoxic events are geologically abrupt phases of extreme oxygen depletion in the oceans that disrupted marine ecosystems and brought about evolutionary turnover. Typically lasting ~1.5 million years, these events occurred frequently during the Mesozoic era, from about 183 to 85 million years ago, an interval associated with continental breakup and widespread large igneous province volcanism. One hypothesis suggests that anoxic events resulted from enhanced chemical weathering of Earth's surface in a greenhouse world shaped by high volcanic carbon outgassing. Here we test this hypothesis using a combination of plate reconstructions, tectonic–geochemical analysis and global biogeochemical modelling. We show that enhanced weathering of mafic lithologies during continental breakup and nascent seafloor spreading can plausibly drive a succession of anoxic events. Weathering pulses collectively gave rise to substantial releases of the nutrient phosphorus to the oceans, stimulating biological primary production. This, in turn, enhanced organic carbon burial and caused widespread ocean deoxygenation on a scale sufficient to drive recurrent anoxia. This model complements volcanic outgassing-centred hypotheses for triggering these events by demonstrating well-quantified basaltic sources of phosphorus release during periods of intense weathering related to climate warmth. Our study highlights a close coupling between the solid Earth and biosphere during continental reorganization.

Oceanic anoxic events (OAEs) are transient perturbations to the global carbon cycle, during which large regions of the oceans are depleted in dissolved oxygen[1,2]. The resulting euxinic (anoxic and sulfidic) waters are highly toxic, leading to biological turnover events and, in extreme cases, mass extinctions of marine biota[2]. For example, the Toarcian OAE (T-OAE) involved an ~70% reduction in the diversity of some benthic fauna[3]. It is widely accepted that OAEs are ultimately linked to global warming[2], which intensifies the hydrological cycle[4] and chemical weathering on the continents[5,6]. These conditions lead to increased primary production and organic matter burial in the oceans[7], documented in the geological record as organic-rich black shales[1] (Fig. 1). These processes, in turn, cause a substantial reduction in deep-water O_2 concentration ($[O_2]$).

Other Phanerozoic OAEs include the Steptoean Positive Carbon Isotope Excursion, the Hirnantian OAE, the Frasnian–Famennian and the Permian/Triassic boundary event[4]. However, the Mesozoic brought multiple OAEs in close succession (Figs. 1 and 2), with a mean duration of 1.4 Myr and a recurrence interval of ~7 Myr (Extended Data Table 1).

[1]School of Ocean and Earth Science, University of Southampton, Southampton, UK. [2]School of Earth and Environment, University of Leeds, Leeds, UK. [3]School of Physics, Chemistry and Earth Sciences, University of Adelaide, Adelaide, South Australia, Australia. [4]Department of Earth and Planetary Sciences, Yale University, New Haven, CT, USA. [5]Yale Institute for Biospheric Studies, Yale University, New Haven, CT, USA. [6]Department of Earth and Environmental Sciences, University of Waterloo, Waterloo, Ontario, Canada. [7]Department of Earth Sciences, Utrecht University, Utrecht, Netherlands. [8]Present address: School of Earth Sciences, University of Bristol, Bristol, UK. ✉e-mail: T.M.Gernon@soton.ac.uk
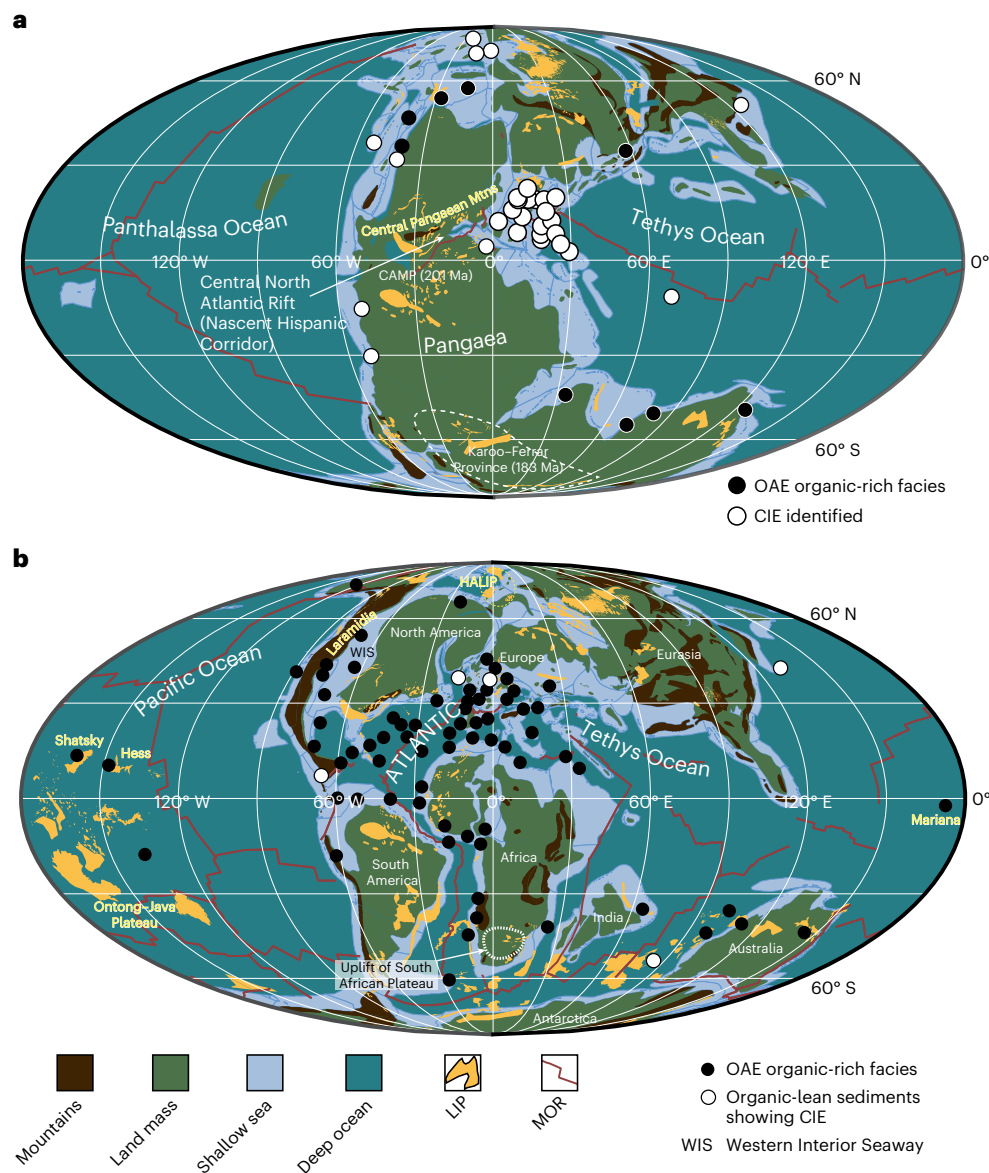
Fig. 1 | Global distribution of OAE sedimentary deposits and plate boundary features. a,b, Plate-tectonic reconstructions (Methods) showing the main palaeogeographic features, MORs and exposed large igneous provinces, as well as the approximate distribution of OAE-related sequences in the Toarcian OAE at about 183–182 Ma (with OAE sites from ref. 49 and references therein) (**a**) and Turonian at about 90 Ma (with OAE sites from ref. 50 and references therein) (**b**). Note that shallow seas include epicontinental seaways, including the Western Interior Seaway of North America. CIE, carbon isotope excursion; HALIP, High Arctic Large Igneous Province. Figure created with GPlates[26] (https://www.gplates.org/).

Earth system models implicate a role for continental configuration in promoting deoxygenation of Mesozoic ocean shelves[8]. However, the interconnected nature of coeval environmental processes, including carbon outgassing from volcanogenic and/or methanogenic sources, global warming, increases in thermohaline circulation and changes in nutrient cycling, leaves the first-order drivers of OAEs open to debate.

OAEs and large igneous provinces

OAE initiation has been attributed to intensified carbon dioxide (CO_2) emissions from large igneous provinces (LIPs)[9,10] (Fig. 1), many of which coincide with known anoxic events (Fig. 2b). Uncertainties in LIP ages, typically ±1 Myr (similar to mean OAE duration), and intervals of activity up to 40 Myr (Fig. 2b)[11] pose challenges for establishing conclusive linkages. A compounding factor is that LIPs are typically associated with continental rifted margins where other geological processes co-occur[12]. There is no doubt, however, that the high frequency of LIPs (Fig. 2b) contributed to the prolonged greenhouse conditions of the late

Mesozoic era that promoted intense chemical weathering. The question is whether LIP emplacement initiates an instantaneous weathering response. Global chemical weathering intensity over the past 400 Myr is only weakly correlated with both the total eruptive area and LIP area within the tropics[6], implicating other factors. However, the influence of LIPs peaks 35–50 Myr after emplacement[6], perhaps indicating a delayed weathering response associated with passive margin rejuvenation[13].

The Mesozoic era brought substantial changes in global ocean chemistry, including several carbon isotope excursions (Fig. 2c–f). These changes do not provide an unambiguous record of the relative magnitude of weathering inputs as geochemical proxies record contributions from multiple, simultaneous geological processes[6]. For example, the gradual increase in seawater $^{87}Sr/^{86}Sr$ (Fig. 2f) reflects increased weathering related to arc volcanism as well as continental breakup[6] (Fig. 2h). Further, the long oceanic residence time of Sr (~5 Myr) limits its utility in identifying OAE drivers. While $^{187}Os/^{188}Os_{initial}$ (Os_i) signatures offer more promise, a substantial osmium input from continental
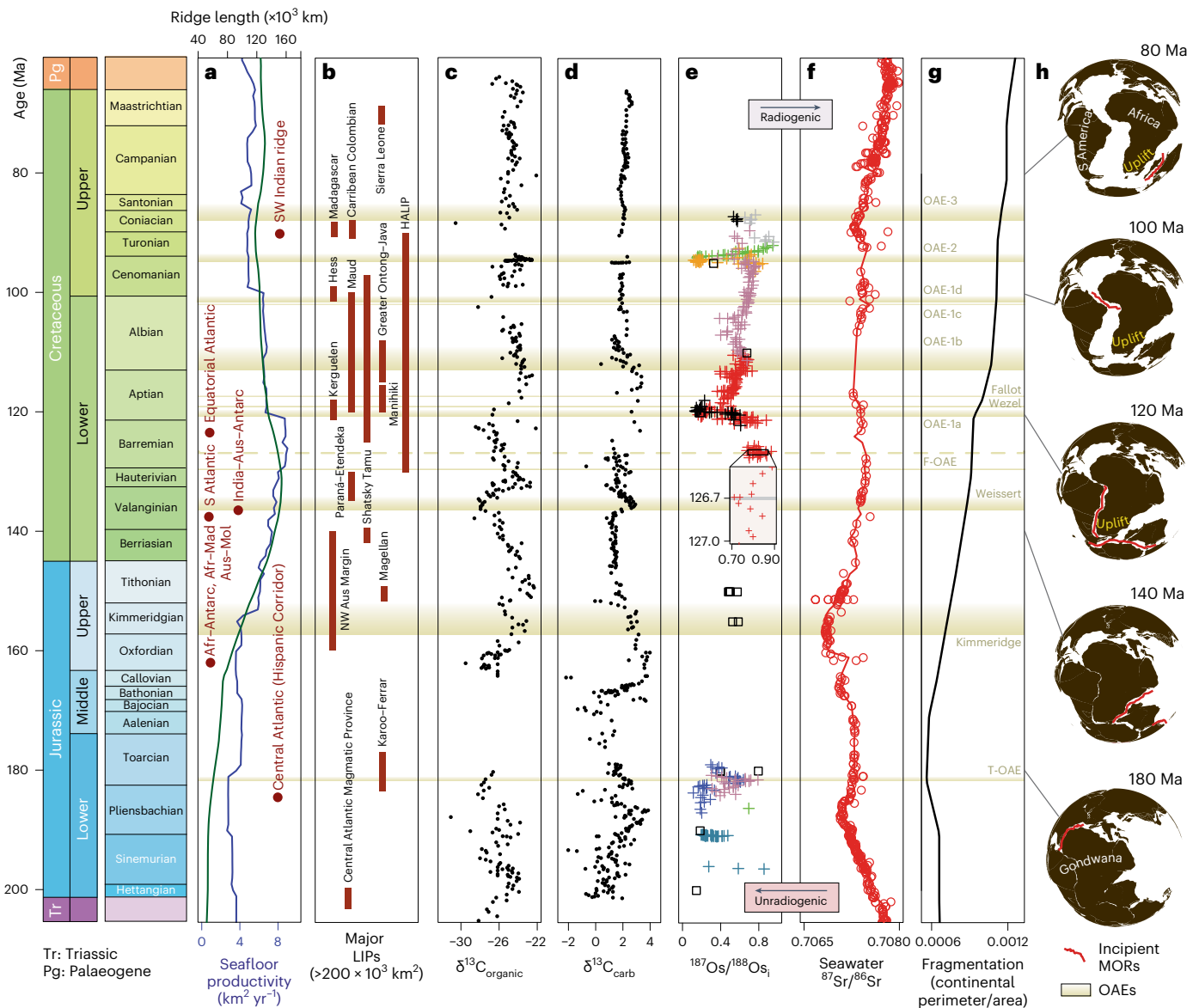
Fig. 2 | Tectonic, magmatic and oceanic chemical changes during the Mesozoic. a, Seafloor production rates (from ref. 6) and total length of MORs and transform faults[51], and major phases of ocean basin formation (onset labelled). OAEs are shown as horizontal beige bands (note that the Kimmeridge is not strictly an OAE, and the dashed line for the Late-Hauterivian Faraoni OAE (F-OAE) is from ref. 52); **b,** LIPs (those with areas of >200 × 10³ km²)[11]; also shown is the revised age range for the Ontong–Java Plateau[53]; **c,** $\delta^{13}C_{organic}$ from organic-rich sediments[54]. **d,** $\delta^{13}C_{carb}$ (inorganic carbon) from marine carbonates[55]. **e,** The $^{187}Os/^{188}Os_i$ signatures of sediments (data sources provided in Extended

Data Table 2). **f,** Seawater $^{87}Sr/^{86}Sr$ ratios from marine carbonates[56]; these ratios gradually increased during the Mesozoic era in step with Gondwana fragmentation (see **h**). **g,** Continental fragmentation index calculated using continental perimeter/area from plate reconstructions[57] (greater values signify a higher degree of fragmentation, and vice versa). **h,** Simplified plate reconstructions showing Gondwana breakup (orthographic projection) on the basis of the Ocean Drilling Stratigraphic Network magnetic reference frame (https://www.odsn.de/). Afr–Antarc, Africa–Antarctica; Afr–Mad, Africa–Madagascar; Aus–Mol, Australia–Molucca.

weathering sources could plausibly mask a volcanic signal (and vice versa), even if volcanism was the first-order driver of global anoxia.

Global tectonic reorganization of the Mesozoic

We propose that processes associated with continental breakup plausibly drove many Mesozoic OAEs (Fig. 2f). Breakup and mid-ocean-ridge assembly reached peak intensity during the major interval of OAEs (Fig. 2a,g,h). The 'rift-to-drift' transition and associated uplift of continental margins generates extensive volcanic terrains, which, in turn, lead to increased weathering of mafic lithologies. Volcanic rocks such as basalts are enriched in phosphorus (P)[14,15], a biolimiting nutrient that regulates burial of organic matter over geological timescales[16]. Enhanced weathering of such rocks supplies nutrients to

oceans, influencing bioproductivity[17,18]. For example, excess delivery of bioavailable P can lead to eutrophic conditions that deplete water column [O₂], causing widespread anoxia or euxinia[19]. Such conditions can be sustained over million-year timescales via further recycling of P from sediments overlain by anoxic or euxinic waters, as indicated by observations[20,21] and models[19,22] of the Cenomanian–Turonian OAE (OAE 2). Like the weathering of mafic rocks on land[15], volcanism during mid-ocean-ridge formation contributes essential nutrients, including P, directly to the global ocean through submarine weathering[14].

Incipient MORs

During the Mesozoic, the breakup of Gondwana (Fig. 2f–g) involved a protracted, ~120-Myr-long episode of mid-ocean-ridge assembly on a

global scale (Figs. 1, 2a and 3). In addition to fragmenting the continents and increasing global weatherability[6], this process generated narrow ocean basins (Figs. 1 and 3a and Extended Data Fig. 1) where restricted water circulation can cause limited ventilation of bottom waters, locally encouraging the expansion of anoxia and euxinia. Although enhanced weathering can increase organic carbon burial, removing atmospheric CO_2 and causing global cooling, this process may be counteracted by the expansion of the global ridge system—increasing net carbon outgassing into the oceanic reservoir[23], contributing to increased dissolved inorganic carbon and driving ocean CO_2 degassing on geologically short timescales[24].

Extensional plate boundaries are a key source of nutrients to the oceans during breakup[14]. When continental rift basins submerge below sea level, it results in extensive magma–seawater interactions and accelerated chemical weathering of volcanic regolith. In such transitional environments, referred to here as incipient mid-ocean ridges (MORs), enhanced volcanism driven by magma–seawater interactions, coupled with low hydrostatic pressures, also promotes the explosive eruption of basalt[25]. To explore the impact of MOR assembly on ocean chemistry, we first investigate the spatial extent of mature continental rifts that transitioned to nascent ridges within relatively shallow ocean basins, defined here as <1,500 m deep (Extended Data Fig. 1 and Methods). We identify nine incipient ridge segments using the plate-tectonic reconstruction software GPlates[26] (https://www.gplates.org/). We find ~26,000 km of MOR initiated during the Jurassic–Cretaceous, 85% of which was simultaneously active from 160 to 120 million years ago (Ma) (Fig. 3b–d). Analysing seafloor production rates along these ridges, we find that the main incipient MORs overlap in timing with the main OAE interval (Fig. 3d). In northern latitudes, this includes a prolonged phase of oceanic anoxia within the Kimmeridgian, which, while not strictly an OAE, is considered one of the most prominent organic carbon burial episodes of the Phanerozoic[27]. During OAE 2, $\delta^{13}C$ excursions—signalling changes in both local and global carbon cycles—are attributed to basalt–seawater interactions[20], consistent with coeval sharp declines in Os_i in marine sediments[28] (Fig. 2e). Here expanded deoxygenation preceded massive organic carbon burial, reflecting dynamic changes in oceanic redox conditions[29].

Within incipient MOR environments, fragmental, glass-rich basalts undergo rapid alteration, releasing a substantial fraction of elements, including phosphorus, into seawater[14] (Extended Data Fig. 2). Further, incipient MORs coincide with the rift-to-drift phase when decompression melting and upwelling of asthenospheric melts tend to be highest[30] and are typically characterized by an order of magnitude increase in magmatic productivity[31]. This phase of seafloor volcanism can plausibly transform large domains of oceanic crust from minor sinks[32] into net sources[14] of phosphate (Fig. 2d–f). Hyaloclastite breccias and other pyroclastic rocks are commonly formed during the transition from continental rifting to seafloor spreading and have been linked to early explosive magma–water interactions during submergence of the spreading axis[25]. For example, during the formation of the Central Atlantic Ridge[33] (Fig. 3a)—which unzipped to create the Hispanic Corridor (Fig. 1a)—a massive wedge of fragmental basaltic rocks was emplaced along the Atlantic margins of North America. With a volume of ~3×10^6 km³, this feature is one of Earth's largest igneous provinces[30].

We use seafloor production data to estimate P release from basalts emplaced along global ridges (Fig. 3). We use modelled lengths and spreading rates for each ridge to calculate seafloor ridge productivity over time (Fig. 3b–c). We simulate a linear decay in fragmentation and phosphorus release during seafloor subsidence, accounting for reduced weathering intensity as the ridge progressively deepens (Methods). This analysis indicates that P release (Fig. 3f and Extended Data Fig. 3) potentially exceeded 3×10^{10} mol yr⁻¹, equivalent to over 75% of the current total reactive P flux from rivers to the oceans (~3.9×10^{10} mol yr⁻¹) (ref. 34).

## Subaerial basalt uplift and weathering

Subaerial basalt weathering can deliver a substantial flux of bioavailable P to the ocean[15], boosting primary production and organic carbon burial and driving global cooling[35]. Box models of oceanic phosphorus, carbon and oxygen cycles have demonstrated that increased P delivery from continents is sufficient to drive OAEs[19]. Alongside our ridge-derived P flux, we propose an additional riverine supply from a well-established phase of tectonic uplift and exhumation across Mesozoic southern Africa[13], which caused rapid denudation of thick subaerial flood basalts[36–38]. Previous thermochronological studies reveal multiple phases of abrupt cooling of rocks that correspond to erosion of approximately 2-km-thick basalts of Karoo-age (~183 Ma) (refs. 36,37,39) (Methods and Fig. 4a–c), long (>30 Myr) after their eruption. A comparison between denudation rates and offshore sediment accumulation[36] indicates that three times more material was eroded than deposited in offshore basins at this time[37]. This deficit has been attributed to intense chemical denudation[37], consistent with humid subtropical climates regionally at this time[40]. This interpretation is supported by two geological observations: (1) coeval deltas dominated by clays derived from weathering of mafic lithologies[37]; (2) widespread chemogenic carbonates in offshore basins, locally >500 m thick and covering ~330,000 km², purportedly derived from Cretaceous basalt alteration[41].

We next estimate the phosphorus release from weathering related to tectonic uplift in southern Africa (Fig. 4b,c and Methods). Here major exhumation occurred between 120 and 85 Ma, with peaks at about 120, 112, 104 and 95 Ma (Fig. 4c), and denudation rates up to 125–175 m Myr⁻¹ have been reported[36]. At this time, basalts encompassed the wider Karoo Basin—as evidenced by thermochronological constraints[37,39], basalt fragments preserved in deeply eroded kimberlite pipes and the present-day footprint of feeder intrusions (Methods). We develop a simple model using existing thermochronological 'best fit' models to drive denudation rates (Fig. 4c), sampling observed P_2O_5 concentrations from a global compilation of Karoo-aged basalts (GeoROC Database; Methods). Our models estimate that P fluxes from the chemical denudation of the basalts potentially reach 3×10^{10} mol yr⁻¹ (Fig. 4d)—a similar magnitude to the present-day dissolved inorganic P input to the ocean[34]. Previous studies have shown that P accumulation rates rise and reach a peak coinciding with the onset of OAE 2 (ref. 21). Our model suggests this could be due at least in part to increased delivery of phosphate from continents, giving rise to increased primary productivity, organic carbon burial and black shale formation[21].

While it is important to recognize the influence of other palaeogeographic features, such as the Central Pangaean Mountains (Fig. 1a), on continental weathering, constructing a fully integrated Earth system model is beyond the scope of our study. Consequently, our estimated phosphorus fluxes for this comparatively well-documented phase of erosion (Fig. 4) should be regarded as conservative minimum estimates. Considering age uncertainties within terrestrial and marine records (typically ±1–2 Myr), we observe good overall correspondence between the timings of peak weathering events and OAE occurrences (Fig. 4c,d). This prompts the question of whether this relationship is coincidental or causal.

Biogeochemical model

To interrogate whether basalt weathering in submarine and subaerial environments could have driven anoxia, we test the influence of phosphorus release events on oceanic $[O_2]$ and examine how their timings relate to OAEs in the geological record (Fig. 2). We incorporate both submarine (Fig. 3 and Extended Data Figs. 3 and 4) and terrestrial (Fig. 4) basalt weathering fluxes (Supplementary Data 2 and 3) into a global biogeochemical model of carbon–oxygen–phosphorus cycles developed by ref. 42 and adapted by ref. 43 (Extended Data Fig. 5). The model divides the ocean into proximal and distal shelf zones, a surface
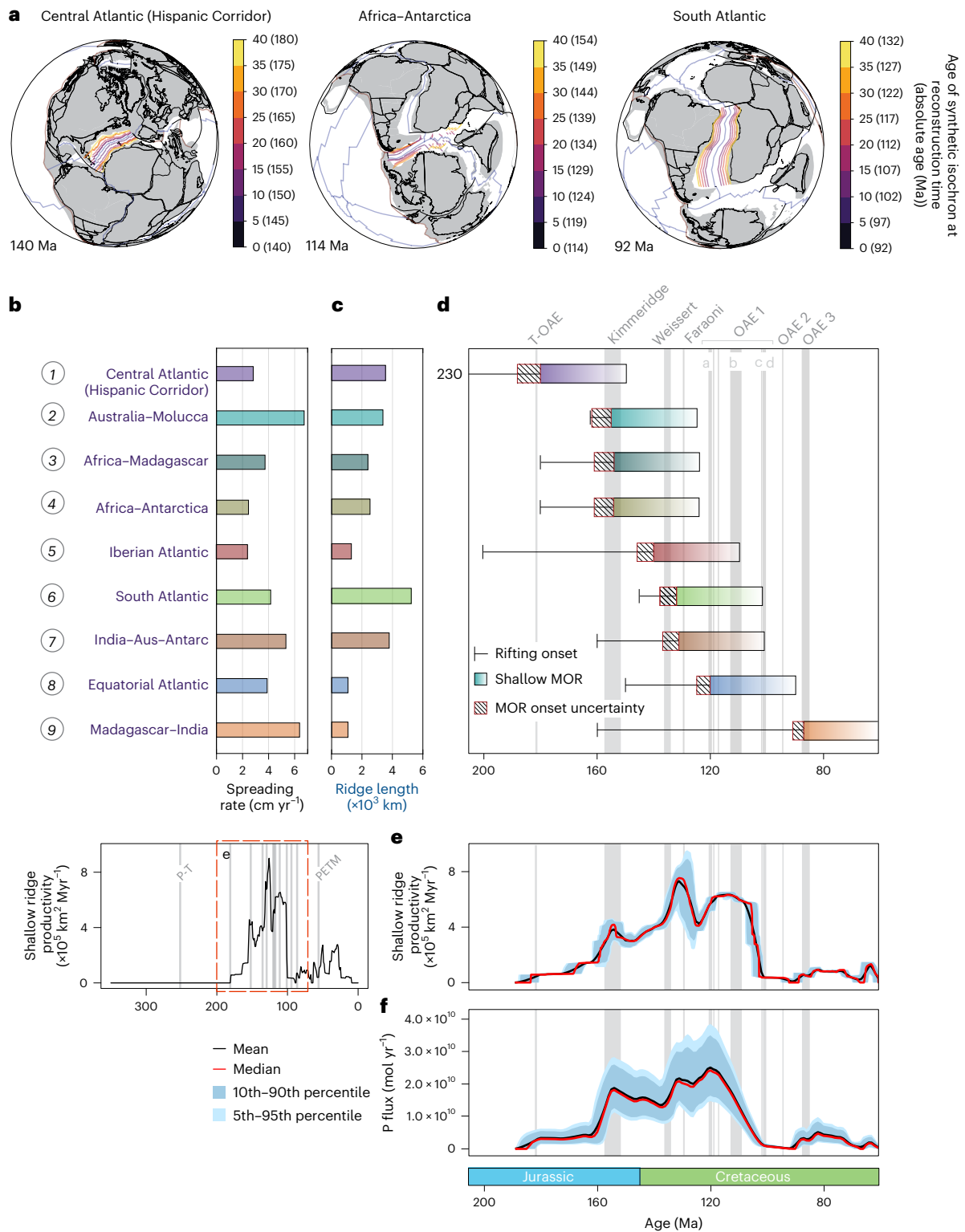
Fig. 3 | Scale of incipient MORs globally during the Mesozoic. a, Plate reconstructions for the Central Atlantic, Africa–Antarctica and South Atlantic incipient MOR systems, with synthetic isochrons showing the time (in Myr) relative to the reconstruction time (labelled; absolute ages in Ma are provided in brackets); see Extended Data Fig. 1 for all active Mesozoic ridge systems. **b,c**, Total ridge length (**b**) and mean full spreading rates for ridges (**c**) based on ref. 58; values shown in **b** and **c** are means for each ridge system over 30 Myr (Methods and Supplementary Data 1). **d**, Summary timeline of shallow ridge volcanism; OAEs are shown as vertical grey bands, and the timing of precursory continental rifting[33] is depicted with horizontal bars. **e**, Summed magmatic productivity of shallow ridges from 200 to 60 Ma incorporating age uncertainty (Methods), assuming water depths of <2 km for 30 Myr (right side); longer-term context back to 350 Ma (left side). **f**, Modelled combined ridge flux of P for all ridges active during this period (Extended Data Figs. 1 and 3), calculated in 10,000 simulations using ridge productivity data shown in **e**. Simulations account for uncertainty in the time of ridge initiation (Methods). P–T, Permo–Triassic anoxic event (linked to Siberian traps LIP); PETM, Palaeocene–Eocene Thermal Maximum (linked to North Atlantic LIP[31]), thought to represent an OAE[2].
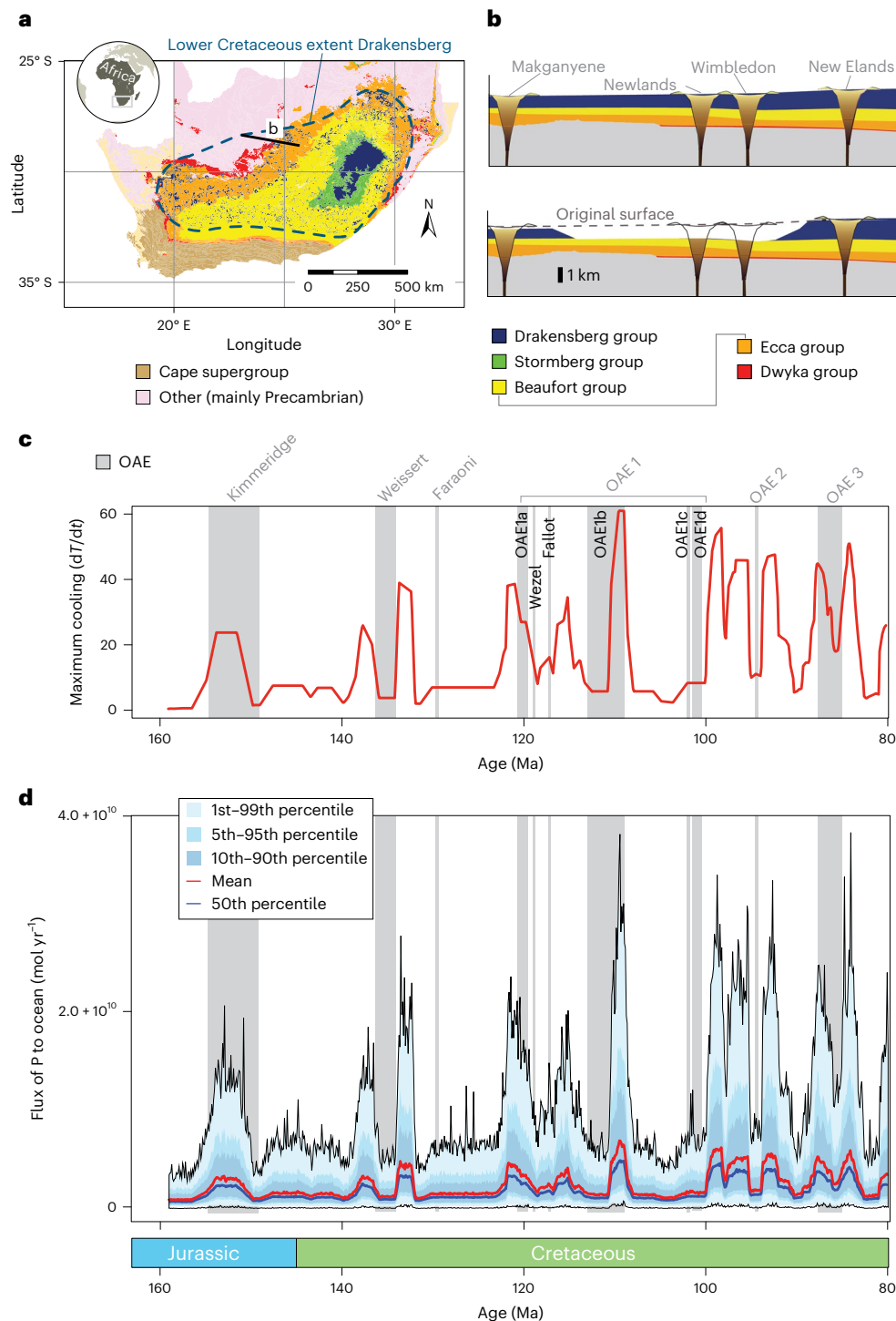
Fig. 4 | Chemical denudation of continental basalts in the Mesozoic.
a, Distribution of Drakensberg basalts and their feeder intrusions (dark blue) within the Karoo Basin of South Africa. **b**, Schematic cross section reconstructions at 120 Ma (top) and -110 Ma (bottom) (line of section in **a**) based on apatite (U–Th)/He thermochronometry[39] and xenoliths in kimberlite pipes. **c**, Estimated cooling rate of rocks across South Africa from thermochronologic models[13] (Methods) related to erosional exhumation between 160 and 80 Ma (hence, age interval shown differs from Fig. 3), showing cooling trends associated with multiple regional events (Methods); the timing of OAEs is shown for context (the earliest event shown, the Kimmeridge (adopting the age of that stage from the International Commision on Stratigraphy, v2023/09), is not strictly an OAE but involved prolonged phases of oceanic anoxia). **d**, Modelled annual flux of P from basalt denudation shown in **a**, utilizing modelled cooling trends from thermochronology for individual localities across southern Africa to drive denudation rate (Methods). Panels **a** and **b** adapted with permission from ref. 39, John Wiley & Sons.

open ocean and a deep ocean interior and explicitly represents primary production and remineralization, as well as the decreasing retention of P in sediments under anoxic conditions[21]. The ridge flux of P is injected into the model's deep ocean box, while the riverine weathering flux is delivered into the proximal shelf zone box. Following ref. 19, we amend

global ocean circulation to account for the warmer, more stagnant ocean of the later Mesozoic. We reduce open ocean vertical mixing to 70% relative to present day, which falls within sensitivity estimates of previous studies[19]. All other background forcings follow the long-term Earth evolution scenario from ref. 43 (Methods).
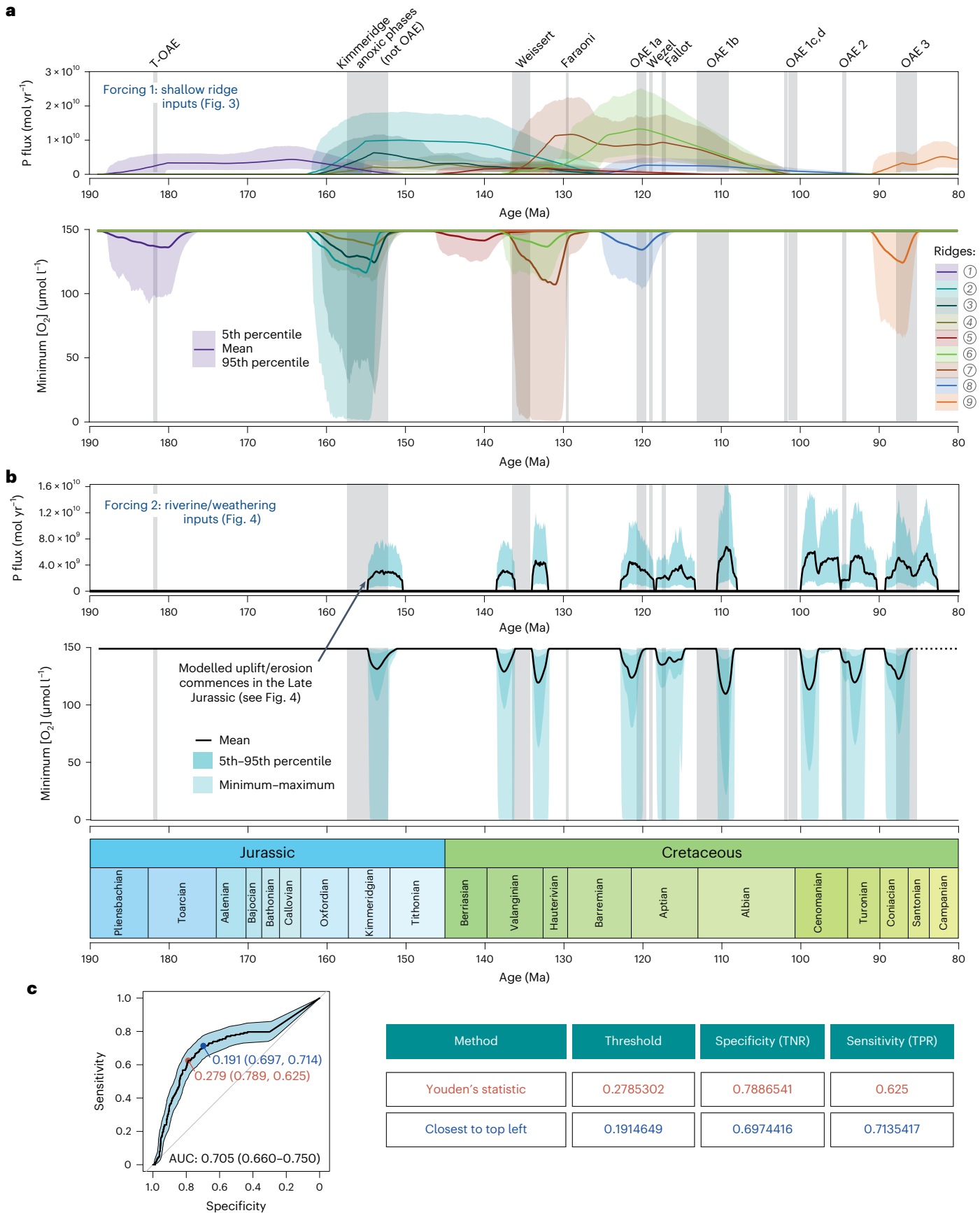
a

b

c

Figure 5 shows model runs through the Jurassic and Cretaceous incorporating both ridge (Fig. 5a and Extended Data Fig. 6) and riverine (Fig. 5b) P fluxes. Each ridge initiation and basalt uplift/weathering event is considered independently (Methods, Fig. 5 and Extended Data Fig. 7) because the biogeochemical model does not yet fully incorporate feedbacks for atmospheric oxygen, for example, terrestrial biosphere and wildfires[44]. Because organic carbon removal means liberation of O_2, later events would be applied in a

Fig. 5 | Modelled ocean deoxygenation through time and observed timing of OAEs. a,b, Mean, 5th–95th percentile and minimum–maximum estimates for dissolved $[O_2]$ in the ocean interior over time from biogeochemical model simulations (see Methods for details). We input multiple (1,000) simulated phosphorus release events for shallow MOR systems (**a**) and riverine (continental weathering) (**b**) sources tied to exhumation in southern Africa during and after Gondwana breakup (Fig. 4); OAEs are shown as vertical grey bands (labelled); upper plots show the P fluxes as discrete events resulting from both processes (see Figs. 3f and 4b for cumulative fluxes). **c**, To evaluate the power of the (normalized) minimum value of $[O_2]$ (see Extended Data Fig. 8) as a predictor of OAEs, we plot an ROC curve, shown. The AUC of 0.705 shows that the $[O_2]$ minima in our models offer reasonably good predictive performance for OAEs in the geological record. The table summarizes true negative rate (TNR) and true positive rate (TPR) for the predictor using two alternative thresholds (Methods).

modified high-oxygen state, which is not consistent with the geological record of broadly stable atmospheric oxygen levels across the Jurassic and Cretaceous[45]. When viewing the model output in these terms, calculated P fluxes and input rates are sufficient to trigger substantial ocean deoxygenation (Extended Data Fig. 7). For T-OAE, our model predicts a prolonged phase of anoxia (Fig. 5a) that conforms with global-scale deoxygenation indicated by marine redox proxies, extending well beyond this event[3,46]. MOR initiation, along with the climate-altering impacts of Karoo–Ferrar volcanism[3,46] (Fig. 2b), can jointly reconcile the long-term unradiogenic Os_i signal bracketing the T-OAE.

The overall correspondence between predicted deoxygenation events and OAEs (Extended Data Table 1) appears moderately good. Modelled drops in $[O_2]$ broadly coincide with 9 out of 11 confirmed OAEs (Fig. 5). Notably, OAEs 1c and 1d do not overlap with either ridge or riverine deoxygenation, occurring approximately 2 Myr before the modelled peak related to riverine inputs (Fig. 5b). Further, OAE 1b occurs ~3 Myr before the modelled peak in deoxygenation. However, it is important to consider the age uncertainties in uplift/weathering events and OAE ages (typically ±1–2 Myr). OAE 2 coincides with an apparently smaller-scale weathering event (Fig. 5). At the Jurassic/Cretaceous boundary, we predict a relatively minor deoxygenation event linked to ridge volcanism, despite no known OAE in this interval (Fig. 5a). To quantify model performance, we apply a simple classifier derived from estimated $[O_2]$ minima to predict OAE occurrence. We identify the minimum value of $[O_2]$ over all individual ridge and weathering model runs (Extended Data Fig. 8) and normalize this to give a value on the interval [0, 1], which can be used as a predictor of OAE occurrence (a binary outcome). Performance is measured using the receiver operating characteristic (ROC) curve (Methods), where the area under the curve (AUC) of 0.705 (95% confidence intervals: 0.660–0.750) signifies a good but imperfect overall predictive value (Extended Data Fig. 8) for OAE timing, outperforming random chance (Fig. 5c).

One feature of the OAE geochemical record that is difficult to reconcile with any model for their origin is the presence of both negative and positive excursions in $\delta^{13}C_{carb}$ (inorganic carbon) values[20] (Fig. 1c,d). In general, increased productivity and eutrophication are expected to yield a positive $\delta^{13}C_{carb}$ signature (for example, OAE 2) as predicted by our model. Hence, the presence of negative $\delta^{13}C$ requires a source of isotopically light carbon. Individual volcanic events may also release light $\delta^{13}C$ if they trigger processes such as permafrost melting and/or thermal metamorphism of mudrocks or coal[47], but this does not negate the role of P release through volcanic weathering in stimulating productivity and causing anoxia/euxinia.

Extent of seafloor anoxia

Our results suggest that most OAEs could be explained by an interplay between enhanced weathering of mafic rocks in submarine and subaerial environments (Fig. 5). Model uncertainty indicates that deoxygenation events yield mean decreases to as little as ~110 µmol kg^{-1} $[O_2]$ averaged across the ocean interior, representing an ~30% decrease in average marine $[O_2]$. As marine $[O_2]$ is difficult to infer for the deep past, most geological estimates of OAE intensity instead focus on the fraction of seafloor overlain by anoxic water. This is also uncertain but appears to be between 1% and 10% of the seafloor for most events[4]. A simple estimation considers that present-day anthropogenic

deoxygenation has reduced mean $[O_2]$ by about 2%, leading to an 85% expansion of anoxic seafloor[48]. Thus, an ~30% reduction in $[O_2]$ is expected to increase seafloor anoxia from the present 0.3% of the ocean floor to about 4%, which is broadly consistent with the magnitude of OAEs in the geological record[4,46]. Modelled probability distributions (Fig. 5a,b) show that basalt weathering can drive much higher degrees of deoxygenation and, in turn, more severe seafloor anoxia (Extended Data Fig. 6).

The proposed weathering mechanisms do not necessarily contradict models for OAE triggering that invoke episodic massive volcanism. Our model quantifies a complimentary source of P that could theoretically drive organic carbon accumulation in marine basins and substantial deoxygenation. This does not preclude the involvement of additional disturbances in the global carbon cycle; rather, it may operate alongside them, if not directly driving OAEs, making oceans more susceptible to anoxia triggering.

To conclude, we hypothesize that continental breakup resulted in elevated background phosphorus levels during the main interval of Mesozoic OAEs (Figs. 2 and 3) sufficiently potent to drive both prolonged and abrupt phases of deoxygenation (Fig. 5). Specifically, multiple pulses of continental basalt weathering linked to Gondwana breakup (Fig. 4) coincide closely in time and magnitude with OAEs (Fig. 5). Both processes plausibly combined to deliver pulsed fluxes of nutrients to the oceans, driving high rates of organic carbon burial and recurrent anoxic events. The Upper Cretaceous decline of this tectono-magmatic activity may help reconcile the frequency and intensity of OAEs in Mesozoic oceans. Our results thus support a mechanistic link between solid Earth processes and anoxic events that caused profound biological turnover episodes[1–3]. The proposed feedbacks between continental reorganization, magmatism and anoxia warrant further investigation and carry implications for understanding the environmental consequences of other breakup events during Earth history.

Online content

Any methods, additional references, Nature Portfolio reporting summaries, source data, extended data, supplementary information, acknowledgements, peer review information; details of author contributions and competing interests; and statements of data and code availability are available at https://doi.org/10.1038/s41561-024-01496-0.

References

1. Jenkyns, H. C. Cretaceous anoxic events: from continents to oceans. *J. Geol. Soc.* **137**, 171 (1980).
2. Jenkyns, H. C. Geochemistry of oceanic anoxic events. *Geochem. Geophys. Geosyst.* **11**, Q03004 (2010).
3. Them, T. R. et al. Thallium isotopes reveal protracted anoxia during the Toarcian (Early Jurassic) associated with volcanism, carbon burial, and mass extinction. *Proc. Natl Acad. Sci. USA* **115**, 6596–6601 (2018).
4. Reershemius, T. & Planavsky, N. J. What controls the duration and intensity of ocean anoxic events in the Paleozoic and the Mesozoic?. *Earth Sci. Rev.* **221**, 103787 (2021).
5. Larson, R. L. & Erba, E. Onset of the mid-Cretaceous greenhouse in the Barremian–Aptian: igneous events and the biological, sedimentary, and geochemical responses. *Paleoceanography* **14**, 663–678 (1999).

6. Gernon, T. M. et al. Global chemical weathering dominated by continental arcs since the mid-Palaeozoic. *Nat. Geosci.* **14**, 690–696 (2021).

7. Arthur, M. A., Schlanger, S. O. & Jenkyns, H. C. The Cenomanian–Turonian Oceanic Anoxic Event, II. Palaeogeographic controls on organic-matter production and preservation. *Geol. Soc. Lond. Spec. Publ.* **26**, 401–420 (1987).

8. Pohl, A. et al. Continental configuration controls ocean oxygenation during the Phanerozoic. *Nature* **608**, 523–527 (2022).

9. Kerr, A. C. Oceanic plateau formation: a cause of mass extinction and black shale deposition around the Cenomanian–Turonian boundary? *J. Geol. Soc.* **155**, 619–626 (1998).

10. Turgeon, S. C. & Creaser, R. A. Cretaceous oceanic anoxic event 2 triggered by a massive magmatic episode. *Nature* **454**, 323–326 (2008).

11. Ernst, R. E. *Large Igneous Provinces* (Cambridge Univ. Press, 2014).

12. Gernon, T. M. et al. Rift-induced disruption of cratonic keels drives kimberlite volcanism. *Nature* **620**, 344–350 (2023).

13. Gernon, T. M. et al. Coevolution of craton margins and interiors during continental break-up. *Nature* **632**, 327–335 (2024).

14. Gernon, T. M., Hincks, T. K., Tyrrell, T., Rohling, E. J. & Palmer, M. R. Snowball Earth ocean chemistry driven by extensive ridge volcanism during Rodinia breakup. *Nat. Geosci.* **9**, 242–248 (2016).

15. Horton, F. Did phosphorus derived from the weathering of large igneous provinces fertilize the Neoproterozoic ocean? *Geochem. Geophys. Geosyst.* **16**, 1723–1738 (2015).

16. Tyrrell, T. The relative influences of nitrogen and phosphorus on oceanic primary production. *Nature* **400**, 525–531 (1999).

17. Zhang, F. et al. Multiple episodes of extensive marine anoxia linked to global warming and continental weathering following the latest Permian mass extinction. *Sci. Adv.* **4**, e1602921 (2018).

18. Percival, L. M. E. et al. Valanginian climate cooling and environmental change driven by Paraná–Etendeka basalt erosion. *Geology* **51**, 753–757 (2023).

19. Tsandev, I. & Slomp, C. P. Modeling phosphorus cycling and carbon burial during Cretaceous oceanic anoxic events. *Earth Planet. Sci. Lett.* **286**, 71–79 (2009).

20. Beil, S. et al. Cretaceous oceanic anoxic events prolonged by phosphorus cycle feedbacks. *Clim. Past* **16**, 757–782 (2020).

21. Mort, H. P. et al. Phosphorus and the roles of productivity and nutrient recycling during oceanic anoxic event 2. *Geology* **35**, 483–486 (2007).

22. Monteiro, F. M., Pancost, R. D., Ridgwell, A. & Donnadieu, Y. Nutrients as the dominant control on the spread of anoxia and euxinia across the Cenomanian–Turonian oceanic anoxic event (OAE2): model–data comparison. *Paleoceanography* **27**, PA4209 (2012).

23. Herbert, T. D. et al. Tectonic degassing drove global temperature trends since 20 Ma. *Science* **377**, 116–119 (2022).

24. Hayes, J. M. & Waldbauer, J. R. The carbon cycle and associated redox processes through time. *Phil. Trans. R. Soc. B* **361**, 931–950 (2006).

25. Planke, S., Symonds, P. A., Alvestad, E. & Skogseid, J. Seismic volcanostratigraphy of large-volume basaltic extrusive complexes on rifted margins. *J. Geophys. Res.* **105**, 19335–19351 (2000).

26. Müller, R. D. et al. GPlates: building a virtual Earth through deep time. *Geochem. Geophys. Geosyst.* **19**, 2243–2261 (2018).

27. Nozaki, T., Kato, Y. & Suzuki, K. Late Jurassic ocean anoxic event: evidence from voluminous sulphide deposition and preservation in the Panthalassa. *Sci. Rep.* **3**, 1889 (2013).

28. Matsumoto, H. et al. Long-term Aptian marine osmium isotopic record of Ontong Java Nui activity. *Geology* **49**, 1148–1152 (2021).

29. Ostrander, C. M., Owens, J. D. & Nielsen, S. G. Constraining the rate of oceanic deoxygenation leading up to a Cretaceous oceanic anoxic event (OAE-2: ~94 Ma). *Sci. Adv.* **3**, e1701020 (2017).

30. Kelemen, P. B. & Holbrook, W. S. Origin of thick, high-velocity igneous crust along the US East Coast margin. *J. Geophys. Res. Solid Earth* **100**, 10077–10094 (1995).

31. Gernon, T. M. et al. Transient mobilization of subcrustal carbon coincident with Palaeocene–Eocene Thermal Maximum. *Nat. Geosci.* **15**, 573–579 (2022).

32. Sharoni, S. & Halevy, I. Rates of seafloor and continental weathering govern Phanerozoic marine phosphate levels. *Nat. Geosci.* **16**, 75–81 (2023).

33. Brune, S., Williams, S. E., Butterworth, N. P. & Müller, R. D. Abrupt plate accelerations shape rifted continental margins. *Nature* **536**, 201–204 (2016).

34. Lenton, T. M., Daines, S. J. & Mills, B. J. W. COPSE reloaded: an improved model of biogeochemical cycling over Phanerozoic time. *Earth Sci. Rev.* **178**, 1–28 (2018).

35. Jenkyns, H. C., Dickson, A. J., Ruhl, M. & van den Boorn, S. H. J. M. Basalt–seawater interaction, the Plenus Cold Event, enhanced weathering and geochemical change: deconstructing Oceanic Anoxic Event 2 (Cenomanian–Turonian, Late Cretaceous). *Sedimentology* **64**, 16–43 (2017).

36. Tinker, J., de Wit, M. & Brown, R. Mesozoic exhumation of the southern Cape, South Africa, quantified using apatite fission track thermochronology. *Tectonophysics* **455**, 77–93 (2008).

37. Stanley, J. R. et al. Constraining plateau uplift in southern Africa by combining thermochronology, sediment flux, topography, and landscape evolution modeling. *J. Geophys. Res. Solid Earth* **126**, e2020JB021243 (2021).

38. Hu, J. et al. Modification of the western Gondwana craton by plume–lithosphere interaction. *Nat. Geosci.* **11**, 203–210 (2018).

39. Stanley, J. R., Flowers, R. M. & Bell, D. R. Erosion patterns and mantle sources of topographic change across the southern African Plateau derived from the shallow and deep records of kimberlites. *Geochem. Geophys. Geosyst.* **16**, 3235–3256 (2015).

40. Burgener, L., Hyland, E., Reich, B. J. & Scotese, C. Cretaceous climates: mapping paleo-Köppen climatic zones using a Bayesian statistical analysis of lithologic, paleontologic, and geochemical proxies. *Palaeogeogr. Palaeoclimatol. Palaeoecol.* **613**, 111373 (2023).

41. Wright, V. P. The mantle, CO_2 and the giant Aptian chemogenic lacustrine carbonate factory of the South Atlantic: some carbonates are made, not born. *Sedimentology* **69**, 47–73 (2022).

42. Slomp, C. P. & Van Cappellen, P. The global marine phosphorus cycle: sensitivity to oceanic circulation. *Biogeosciences* **4**, 155–171 (2007).

43. Alcott, L. J., Mills, B. J. W. & Poulton, S. W. Stepwise Earth oxygenation is an inherent property of global biogeochemical cycling. *Science* **366**, 1333–1337 (2019).

44. Tostevin, R. & Mills, B. J. W. Reconciling proxy records and models of Earth's oxygenation during the Neoproterozoic and Palaeozoic. *Interface Focus* **10**, 20190137 (2020).

45. Mills, B. J. W., Krause, A. J., Jarvis, I. & Cramer, B. D. Evolution of atmospheric O_2 through the Phanerozoic, revisited. *Ann. Rev. Earth Planet. Sci.* **51**, 253–276 (2023).

46. Them II, T. R. et al. Reduced marine molybdenum inventory related to enhanced organic carbon burial and an expansion of reducing environments in the Toarcian (Early Jurassic) Oceans. *AGU Adv.* **3**, e2022AV000671 (2022).

47. Stanley, S. M. Relation of Phanerozoic stable isotope excursions to climate, bacterial metabolism, and major extinctions. *Proc. Natl Acad. Sci. USA* **107**, 19185–19189 (2010).

48. Cheung, W. W. L. et al. in *Special Report on the Ocean and Cryosphere in a Changing Climate* (eds Pörtner, H.-O. et al.) 447–587 (Cambridge Univ. Press, 2019); https://doi.org/10.1017/9781009157964.007

49. Them, T. R. et al. High-resolution carbon isotope records of the Toarcian oceanic anoxic event (Early Jurassic) from North America and implications for the global drivers of the Toarcian carbon cycle. *Earth Planet. Sci. Lett.* **459**, 118–126 (2017).

50. Trabucho Alexandre, J. et al. The mid-Cretaceous North Atlantic nutrient trap: black shales and OAEs. *Paleoceanography* **25**, PA4201 (2010).

51. Merdith, A. S. et al. A full-plate global reconstruction of the Neoproterozoic. *Gondwana Res.* **50**, 84–134 (2017).

52. Matsumoto, H., Coccioni, R., Frontalini, F., Shirai, K. & Kuroda, J. Osmium isotopic evidence for eccentricity-paced increases in continental weathering during the latest Hauterivian, Early Cretaceous. *Geochem. Geophys. Geosyst.* **22**, e2021GC009789 (2021).

53. Davidson, P. C., Koppers, A. A. P., Sano, T. & Hanyu, T. A younger and protracted emplacement of the Ontong Java Plateau. *Science* **380**, 1185–1188 (2023).

54. Falkowski, P. G. et al. The rise of oxygen over the past 205 million years and the evolution of large placental mammals. *Science* **309**, 2202–2204 (2005).

55. Saltzman, M. R. & Thomas, E. Carbon isotope stratigraphy. In *The Geologic Time Scale* (eds. Gradstein, F. M. et al.) 207–232 (Elsevier, 2012).

56. Veizer, J. et al. [87]Sr/[86]Sr, δ^{13}C and δ^{18}O evolution of Phanerozoic seawater. *Chem. Geol.* **161**, 59–88 (1999).

57. Merdith, A. S., Williams, S. E., Brune, S., Collins, A. S. & Müller, R. D. Rift and plate boundary evolution across two supercontinent cycles. *Global Planet. Change* **173**, 1–14 (2019).

58. Müller, R. D. et al. Ocean basin evolution and global-scale plate reorganization events since Pangea breakup. *Ann. Rev. Earth Planet. Sci.* **44**, 107–138 (2016).

Methods

Quantitative estimation of seafloor production rates

To calculate seafloor production rates, we used the plate model of ref. 58, with some corrections as outlined in ref. 59. This plate model comprises a digital repository of continents and plate boundaries and, through a series of Euler rotations, tracks how they have evolved through time. For the Mesozoic–Cenozoic, they are based predominantly on the seafloor spreading history preserved in ocean basins[60].

In our analysis, we use the Python library pyGPlates (gplates. org/docs/pygplates/index.html) to extract all MORs where seafloor spreading occurred, and their associated kinematic data, from the plate model. This includes the length of spreading segments, the rate of spreading, start and end time of activity and the reconstructed position (the latitude and longitude of the MOR), among other metadata. Overall seafloor production rates—a measure of the area in kilometres squared of new seafloor formed along MORs per million years—are calculated by summing the product of spreading rate and spreading segment length for each individual length of the global ridge system. We then export the entire dataset to individual .csv files for each 1 Myr time step between 200 and 0 Ma.

Using the plate-tectonic reconstruction software GPlates[26] (https:// www.gplates.org/), we defined bounding polygons around incipient MOR systems that evolved from a continental rift (in a region of thick continental lithosphere; Extended Data Fig. 1). In our model, these polygons are active for the first 30 Myr of spreading, when the incipient ridge is mostly still relatively shallow and susceptible to enhanced weathering (Main). Nevertheless, we apply a linear decay in fragmentation and phosphorus release during seafloor subsidence (as discussed in the following), which accounts for reduced weathering intensity as the ridge progressively deepens in our model. Spatially, the polygons are defined around congruent geographic regions representing incipient ocean basins. These geographic regions do not always map well to present day; for example, the opening of the Atlantic Ocean is divided into Northern, Iberian, Central, Equatorial and Southern ridge segments. The oceanic ridge systems included in our analysis, with accepted start times in brackets, are as follows: Central Atlantic (180 Ma), Australia–Molucca (155 Ma), Africa–Madagascar (154 Ma), Africa–Antarctica (154 Ma), Iberian Atlantic (140 Ma), South Atlantic (132 Ma), India–Australia–Antarctica (131 Ma), Equatorial Atlantic (120 Ma) and India–Madagascar (87 Ma). These data are summarized in Fig. 3a–d and Extended Data Fig. 1 and are supplied in Supplementary Data 1.

The preceding analysis yields a series of polygons that spatially and temporally define the limits of incipient MORs and a series of datasets describing all active ridges at a specified time step. We use the 'select' function of the Generic Mapping Tools (https://www. generic-mapping-tools.org/) software, which intersects datasets (including .csv files with latitude/longitude coordinates) against a polygon(s) to extract data within the polygon at each time step per bounding box (at their active times). This gives us individual time series (multiple .csv files) of the ridge segments within each bounding box that we merge into individual profiles for each discrete ocean basin.

Mapping OAEs

Figure 1 plots the location of organic-rich facies and carbon isotope excursions of the two major OAEs, T-OAE and OAE 2. These locations were previously compiled by ref. 49 for T-OAE (building on the earlier compilation of ref. 61) and ref. 50 for OAE 2. The maps were produced using the open-source plate-tectonic reconstruction software GPlates, using the palaeogeographic regions of ref. 62 and the plate rotations of ref. 63. The distribution of large igneous provinces was plotted using the shapefiles of ref. 64.

Modelling shallow MOR phosphorus release

To estimate the flux of phosphorus into the ocean from fragmented basaltic materials emplaced along shallow incipient MORs (Extended

Data Fig. 1), we adapted models from ref. 14, which probabilistically estimate elemental fluxes from the chemical weathering of seafloor basalts, accounting for uncertainties in parameters. Because seafloor production is reasonably well constrained for the Jurassic and Cretaceous[58,65], we used seafloor production data (acquired using the preceding procedures) in our models. These data include estimates for seafloor production rates ($km^2 Myr^{-1}$), total ridge length (km) and mean spreading rate ($km Myr^{-1}$) globally at 1 Myr intervals. The nine ridges considered in this analysis, listed in the preceding (Fig. 3a,d), are shown in Extended Data Fig. 1 (Supplementary Data 1). We define 'shallow' as water depths of 1,500 m or less. We also consider durations for ridge productivity of up to 30 Myr after ridge initiation, a period during which the ridge should be at its shallowest[66,67], particularly in the presence of dynamic support. To account for age uncertainty associated with the timing of ridge formation, we apply a random offset to the start time (t_s) of each ridge (Fig. 3e), sampling from a beta distribution scaled to the interval [0, 0.05 t_s]. This approach simulates uncertainty that increases further back in time[6], up to 5% of t_s. We use beta parameters $\alpha = 1$, $\beta = 1.5$ (skewed towards zero), which corresponds to a mean offset of 2%, and standard deviation of approximately 1.3%.

Our model estimates the volume of fragmental basaltic material over time for each rift/ridge segment (Main). We assume that the total thickness of this material formed and accessed by seawater infiltration will decrease over the duration considered in the model runs. This assumption is considered reasonable because (1) higher magmatic productivity is expected at the earliest stages during ridge initiation due to decompression melting and active upwelling of asthenosphere[30,31,68], which typically coincides with (2) initially shallow water conditions that favour more intense hydrovolcanism (for example, hyaloclastite formation)[25] and pyroclastic eruptions[14]; (3) when new seafloor subsides and is transported away from the ridge it cools and is expected to experience less vigorous convection by infiltrating seawater and hydrothermal flow processes[69,70]. Therefore, we simulate a simple linear decay in thickness of fragmental material over time, from 1,500 m to 100 m over the model run, values that are considered realistic on the basis of observations of seafloor hydrothermal systems[14,69]. We apply ranges of values for shallow and deep porosity, hyaloclastite abundance and palagonite fraction[71] used in previous models[14]. We also used element loss estimates from ref. 14, based on ref. 71 (Extended Data Fig. 2), yielding the following uniform distributions: P_2O_5 loss: [0.002, 0.006]. In our calculations, we use a standard density of 2,390 kg m^{-3} for P_2O_5.

We performed 10,000 individual calculations to build an output distribution that captures the estimated uncertainty in model parameters and timing of ridge initiation. For each iteration, we step through each ridge in turn, sampling palagonite fraction, shallow/deep porosity, hyaloclastite fraction and element losses (specifically, in our case, P_2O_5). Then, for each ridge, we step through the active period at 1 Myr intervals. At each time step from $t = 0$ (when the ridge first becomes active), we use the ridge production values and alteration depth (using the linear decay model) from the input file. The absolute event timing is modified for each ridge at each iteration using a sampled offset (explained in the preceding), and the time series are finally interpolated to regular 1 Myr intervals before being combined with the results from all ridges and model iterations.

We next calculated hyaloclastite thickness as a function of alteration depth and sampled hyaloclastite fractions. By multiplying hyaloclastite thickness by ridge production, we then calculate the total hyaloclastite volume and hyaloclastite weight. The total weight of P_2O_5 released is the weight of hyaloclastite multiplied by the randomly sampled palagonite fraction and P_2O_5 loss (using the distributions given in the preceding). We then convert to moles P as a total flux into the ocean per 1 Myr.

This procedure gives 10,000 individual (offset) time series for P for each ridge. We performed linear interpolation of each (offset) time series to estimate the total P (mol) released from each ridge at regular

1 Myr time steps from 180 to 59 Ma (Extended Data Fig. 3). Then, for each individual iteration, we calculated the total mol P from all active ridges. This gives 10,000 variant time series for total estimated mol P. From this we can then calculate the mean, median and percentile estimates at each time step (5th, 10th, 90th and 95th percentile mol P). The resulting time series for mol P, and associated uncertainty, is shown in Fig. 3f. These data are supplied in Supplementary Data 2.

Modelling continental denudation

In addition to incipient MORs, we simulate the phosphorus contribution from a major phase of uplift and denudation that occurred across southern Africa from about 160 to 80 Ma (Main). This denudation involved basaltic lavas of the ~183 Ma Karoo Group[72]. The present-day Drakensberg Mountains in Lesotho are a relic of this thick basaltic sequence, which during the Cretaceous period extended much farther to the west[39]. We sought to quantitatively estimate the amount of P liberated during chemical denudation of these basalts in this interval. To do this, we turned to thermochronology, which provides constraints on the spatial and temporal extent and magnitude of crustal cooling and thus exhumation (uplift and denudation). These cooling history models[36,37,39,73–80] cover a large area of southern Africa owing to the availability of well-dated kimberlite pipes.

We used the rate of change of temperature (cooling rates) from previous thermochronology studies for 28 individual localities spanning southern Africa, using best-fit thermal histories defined in those studies[13]. These are temporally irregularly spaced observations/measurements, so we interpolate to give regular time series with a 0.1 Myr interval (a linear interpolation using the R approx() function). We extend all time series to span the period 160 to 55 Ma using the first and last observed values to pad the series as required.

For each locality we use the R function rollapply() to calculate the change in temperature T over a 1.9 Myr symmetric (rectangular) moving window:

$$\Delta T / \Delta t_{1.9\text{Myr}(t)} = \frac{(T(t-0.9) - T(t+0.9))}{1.9}$$

This is the estimated temperature drop occurring at time t over the window $t \pm 0.9$ Myr. Note that the total width is an odd number as we require a symmetric window. At each 0.1 Myr time step, t (from 160 to 55 Ma), we then find the maximum value of $\Delta T / \Delta t_{1.9\text{Myr}}$ over all the localities and save this as a separate time series (max($f(t)$), where $f(t)$ = maximum temperature drop over all localities at a given time step, t). This is then used to estimate the denudation rate and quantitatively compute how this varies over time.

We assume a minimum denudation rate $D_{min} = 20$ m Myr^{-1}, and maximum rate $D_{max} = 175$ m Myr^{-1}, on the basis of previously reported denudation rates in this region spanning this interval and underpinned by thermochronology and offshore sediment accumulation histories[36]. We make the simplifying assumption that the denudation rate scales linearly with the rate of temperature drop—the estimated maximum ΔT at each time step. This means we have a denudation rate $D = 20$ m Myr^{-1} where ΔT is at its minimum (min$_{\Delta T}$ = min(f) over the period of interest) and a denudation rate $D = 175$ m Myr^{-1} where ΔT is at its maximum (max$_{\Delta T}$ = max(f)). The scaling factor S_D for denudation is then computed as follows:

$$\text{Dscale}(t) = \frac{(f(t) - \text{min}_{\Delta T})}{(\text{max}_{\Delta T} - \text{min}_{\Delta T})}$$

$$\text{Denudation}, D = D_{min} + (S_D \times (D_{max} - D_{min}))$$

$$\text{Eroded}_{\text{vol}(t)} = \text{Basalt}_{\text{area}} \times (\text{Denudation}(t)/1,000)$$

The variable Basalt_area denotes the spatial extent of basalts in the Drakensberg Group. This area is estimated as 600,000 km^2 on the

basis of thermochronology models[39,73], fragments of basalt preserved in deeply eroded kimberlite pipes[81] and the present-day spatial footprint of intrusions that served as feeders to flood basalt eruptions[72] (Fig. 4a). We convert denudation rate from m Myr^{-1} to km Myr^{-1} to give the total volume in km^3 Myr^{-1}. We can then estimate how much phosphorus this potentially involves.

To estimate P_2O_5 contents of the weathered basalts, we sample from a large database, obtained from the GeoRoc repository (https://georoc.eu/), of measured P_2O_5 contents from basalts of the Karoo and age-equivalent Ferrar Provinces. We used this dataset as an empirical distribution for P_2O_5 in our models instead of fitting an arbitrary distribution. We performed 10,000 iterations to build an output distribution for output P (Mol) over time. The P_2O_5 dataset has a total of 2,495 observations (latitude, longitude and P_2O_5 content as a percentage, ranging from >0 to 5.39%), and we exclude a small number of cases (36) with zero P_2O_5 contents. The estimated phosphorus fluxes from each of the nine continental weathering 'events' considered are supplied in Supplementary Data 3.

Biogeochemical modelling of the effects of P inputs

To test the effects of P input into the ocean through incipient seafloor ridges and continental basaltic weathering, we use the five-box ocean–atmosphere model of ref. 43. The model tracks the long-term evolution of the carbon, phosphorus and oxygen cycles over Earth history and was extended from a model originally developed to investigate Mesozoic OAEs[42]. In this study, we use the standard run of the model but impose phosphorus input events on the basis of our data compilation for ocean ridges (Fig. 3) and continental denudation events (Fig. 4). We include the sluggish open ocean upwelling based on previous uses of this model to investigate OAEs[42]. P input from ridges is delivered into the 'Deep ocean' box as soluble reactive phosphorus. P input from weathering is delivered into the 'proximal zone' box of the continental margin, again as soluble reactive phosphorus (Extended Data Fig. 5). We track the model response to these input forcings by plotting the deep ocean [O$_2$] concentration (Fig. 5a,b, Extended Data Fig. 7 and Supplementary Data 4). Although we produce estimates of the combined P inputs over the Mesozoic, we test each input event in the model individually. This is because the model lacks powerful feedbacks on atmospheric oxygen levels associated with the land biosphere, and thus combined long-term increases in P inputs can raise atmospheric O$_2$ to high levels that are no longer consistent with a Mesozoic background state.

Evaluating the predictive performance of biogeochemical models

Here we outline the methodology used to assess the predictive power of the minimum value of [O$_2$] in our biogeochemical models (Fig. 5) as an indicator for the timing of OAEs in the geological record (Extended Data Table 1). To generate a single predictive measure from separate model runs, we first computed the mean output for the weathering and individual ridge model simulations (Fig. 5; note each ridge is simulated separately). At each time step, we identified the overall minimum value of [O$_2$], selecting the lowest value from either the ridge model (Fig. 5a) or the riverine/weathering model (Fig. 5b). This allows us to derive a single measure from multiple, separate model runs (Extended Data Fig. 8a), mitigating the need to use arbitrary thresholds to define 'lows' in [O$_2$] levels.

We then normalized this derived time series (Extended Data Fig. 8a) to the interval [0,1] and inverted the values (1 – normalized value). This yields a simple predictor for OAE events (a binary outcome), allowing us to test the hypothesis that values closer to 1 (corresponding to the [O$_2$] minima) indicate a higher probability of OAE occurrence. This normalized and inverted time series is shown in Extended Data Fig. 8b.

To evaluate the predictive performance of this model, we plotted an ROC curve (Fig. 5c), which shows the trade-off between sensitivity

(the true positive rate—the probability of predicting an OAE event given an actual OAE event) and specificity (the true negative rate, correctly predicting the absence of an OAE event) for a range of classification thresholds. The AUC provides a measure of the forecast performance: a random, no-skill forecast would follow the diagonal line with an AUC of 0.5, and a perfect classifier would have an AUC of 1 (perfect sensitivity and specificity). The 95% confidence intervals are computed from 2,000 stratified bootstrap samples using the R package, pROC[82] (CRAN.R-project.org/package=pROC). The ROC plot (Fig. 5c) shows that the simple classifier (described in the preceding) derived from modelled [O_2] minima (Extended Data Fig. 8) is a reasonably good predictor of OAEs in the geological record, surpassing random chance.

Two examples of potential diagnostic thresholds are given in Fig. 5c (corresponding to Extended Data Fig. 8). Youden's J statistic[83] (red text/line) defines the optimal cut-off as the threshold value that maximizes the distance to the diagonal. 'Closest to top left' (blue) minimizes the distance from the top left corner (the point corresponding to perfect sensitivity and specificity). Classifier values over a given threshold correspond to a prediction of an OAE event occurring, and values below the threshold predict no OAE.

As shown in the right-hand panel of Fig. 5c, using the threshold 0.19 gives a true positive rate (TPR) of 0.71; this is higher than using the Youden method (TPR 0.625), but at a cost of a lower true negative rate (TNR 0.70 versus 0.79 for the Youden method). In practice, the relative cost of a false alarm or miss would be evaluated to determine the optimal threshold.

Data availability

All data generated or analysed during this study are provided in Source Data files and Extended Data Tables 1 and 2. All model outputs are available via figshare at https://doi.org/10.6084/m9.figshare.24153351 (ref. 84). Source data are provided with this paper.

Code availability

The computational codes used for the plate-tectonic modelling are available via GitHub at the following link: https://github.com/amer7632/Gernon_OAE_workflows. The code for the biogeochemical models is available via GitHub at the following link: https://github.com/bjwmills/Gernon2024.

References

59. Torsvik, T. H. et al. Pacific–Panthalassic reconstructions: overview, errata and the way forward. *Geochem. Geophys. Geosyst.* **20**, 3659–3689 (2019).

60. Seton, M. et al. Global continental and ocean basin reconstructions since 200 Ma. *Earth Sci. Rev.* **113**, 212–270 (2012).

61. Jenkyns, H. C. The early Toarcian (Jurassic) anoxic event; stratigraphic, sedimentary and geochemical evidence. *Am. J. Sci.* **288**, 101–151 (1988).

62. Cao, W. et al. Improving global paleogeography since the late Paleozoic using paleobiology using paleobiology. *Biogeosciences* **14**, 5425–5439 (2017).

63. Müller, R. D. et al. A global plate model including lithospheric deformation along major rifts and orogens since the Triassic. *Tectonics* **38**, 1884–1907 (2019).

64. Johansson, L., Zahirovic, S. & Müller, R. D. The interplay between the eruption and weathering of large igneous provinces and the deep-time carbon cycle. *Geophys. Res. Lett.* **45**, 5380–5389 (2018).

65. Müller, R. D., Sdrolias, M., Gaina, C. & Roest, W. R. Age, spreading rates, and spreading asymmetry of the world's ocean crust. *Geochem. Geophys. Geosyst.* **9**, Q04006 (2008).

66. Parsons, B. & Sclater, J. G. An analysis of the variation of ocean floor bathymetry and heat flow with age. *J. Geophys. Res.* **82**, 803–827 (1977).

67. Cochran, J. R. & Buck, W. R. Near-axis subsidence rates, hydrothermal circulation, and thermal structure of mid-ocean ridge crests. *J. Geophys. Res. Solid Earth* **106**, 19233–19258 (2001).

68. Storey, M., Duncan, R. A. & Tegner, C. Timing and duration of volcanism in the North Atlantic Igneous Province: implications for geodynamics and links to the Iceland hotspot. *Chem. Geol.* **241**, 264–281 (2007).

69. Alt, J. C. in *Seafloor Hydrothermal Systems: Physical, Chemical, Biological, and Geological Interactions* (eds Humphris, R. A. et al.) 85–114 (AGU, 1995).

70. Mottl, M. J. & Wheat, C. G. Hydrothermal circulation through mid-ocean ridge flanks: fluxes of heat and magnesium. *Geochim. Cosmochim. Acta* **58**, 2225–2237 (1994).

71. Stroncik, N. A. & Schmincke, H. U. Palagonite—a review. *Int. J. Earth Sci.* **91**, 680–697 (2002).

72. Council for Geoscience *Geologic Map of South Africa, 1:1M* (National Science Councils of South Africa, 2016).

73. Stanley, J. R., Flowers, R. M. & Bell, D. R. Kimberlite (U–Th)/He dating links surface erosion with lithospheric heating, thinning, and metasomatism in the southern African Plateau. *Geology* **41**, 1243–1246 (2013).

74. Brown, R. W., Summerfield, M. A. & Gleadow, A. J. W. Denudational history along a transect across the Drakensberg Escarpment of southern Africa derived from apatite fission track thermochronology. *J. Geophys. Res. Solid Earth* **107**, ETG 10-1–ETG 10-18 (2002).

75. Stanley, J. R. & Flowers, R. M. Mesozoic denudation history of the lower Orange River and eastward migration of erosion across the southern African Plateau. *Lithosphere* **12**, 74–87 (2020).

76. Kounov, A., Viola, G., de Wit, M. & Andreoli, M. A. G. Denudation along the Atlantic passive margin: new insights from apatite fission-track analysis on the western coast of South Africa. *Geol. Soc. Spec. Publ.* **324**, 287–306 (2009).

77. Kounov, A., Viola, G., Dunkl, I. & Frimmel, H. E. Southern African perspectives on the long-term morpho-tectonic evolution of cratonic interiors. *Tectonophysics* **601**, 177–191 (2013).

78. Wildman, M. et al. Post break-up tectonic inversion across the southwestern cape of South Africa: new insights from apatite and zircon fission track thermochronometry. *Tectonophysics* **654**, 30–55 (2015).

79. Wildman, M. et al. Contrasting Mesozoic evolution across the boundary between on and off craton regions of the South African Plateau inferred from apatite fission track and (U–Th–Sm)/He thermochronology. *J. Geophys. Res. Solid Earth* **122**, 1517–1547 (2017).

80. Green, P. F., Duddy, I. R., Japsen, P., Bonow, J. M. & Malan, J. A. Post-breakup burial and exhumation of the southern margin of Africa. *Basin Res.* **29**, 96–127 (2017).

81. Hanson, E. K. et al. Cretaceous erosion in central South Africa: evidence from upper-crustal xenoliths in kimberlite diatremes. *South Afr. J. Geol.* **112**, 125–140 (2009).

82. Robin, X. et al. pROC: an open-source package for R and S+ to analyze and compare ROC curves. *BMC Bioinform.* **12**, 77 (2011).

83. Youden, W. J. Index for rating diagnostic tests. *Cancer* **3**, 32–35 (1950).

84. Gernon, T. M. et al. Model outputs for 'Solid Earth forcing of Mesozoic oceanic anoxic events'. *figshare* https://doi.org/10.6084/m9.figshare.24153351 (2024).

85. Zhou, Z. & Fyfe, W. S. Palagonitization of basaltic glass from DSDP Site 335, Leg 37; textures, chemical composition, and mechanism of formation. *Am. Mineral.* **74**, 1045–1053 (1989).

86. Handoh, I. C. & Lenton, T. M. Periodic mid-Cretaceous oceanic anoxic events linked by oscillations of the phosphorus and oxygen biogeochemical cycles. *Glob. Biogeochem. Cycles* **17**, 1092 (2003).

87. Cohen, K. M., Harper, D. A. T. & Gibbard, P. L. ICS International Chronostratigraphic Chart 2022/10 (ICS and IUGS, 2022); www.stratigraphy.org

88. Mattioli, E., Pittet, B., Riquier, L. & Grossi, V. The mid-Valanginian Weissert Event as recorded by calcareous nannoplankton in the Vocontian Basin. *Palaeogeogr. Palaeoclimatol. Palaeoecol.* **414**, 472–485 (2014).

89. Wouters, S. et al. Progressive increase in organic-matter burial and preservation from the 'Weissert' event to the Faraoni event in Umbria–Marche (central Italy). In *Proc. 6th International Geologica Belgica Meeting* (KU Leuven, 2018).

90. Rodríguez-Tovar, F. J. & Uchman, A. The Faraoni event (latest Hauterivian) in ichnological record: the Río Argos section of southern Spain. *Cretac. Res.* **79**, 109–121 (2017).

91. Jenkyns, H. C. Transient cooling episodes during Cretaceous oceanic anoxic events with special reference to OAE 1a (early Aptian). *Phil. Trans. R. Soc. A* **376**, 20170073 (2018).

92. Leckie, R. M., Bralower, T. J. & Cashman, R. Oceanic anoxic events and plankton evolution: biotic response to tectonic forcing during the mid-Cretaceous. *Paleoceanography* https://doi.org/10.1029/2001PA000623 (2002).

93. Millán, M. I., Weissert, H. J. & López-Horgue, M. A. Expression of the late Aptian cold snaps and the OAE1b in a highly subsiding carbonate platform (Aralar, northern Spain). *Palaeogeogr. Palaeoclimatol. Palaeoecol.* **411**, 167–179 (2014).

94. Friedrich, O., Bornemann, A., Norris, R. D., Erbacher, J. & Fiebig, J. Changes in tropical Atlantic surface-water environments inferred from late Albian planktic foraminiferal assemblages (ODP Site 1258, Demerara Rise). *Cretac. Res.* **87**, 74–83 (2018).

95. Núñez-Useche, F., Barragán, R., Moreno-Bedmar, J. A. & Canet, C. Mexican archives for the major Cretaceous oceanic anoxic events. *Boletín de la Sociedad Geológica Mexicana* **66**, 491–505 (2014).

96. Kouamelan, K. S. et al. Multifractal characterization of the Coniacian–Santonian OAE3 in lacustrine and marine deposits based on spectral gamma ray logs. *Sci. Rep.* **10**, 14363 (2020).

97. Matsumoto, H. et al. Mid-Cretaceous marine Os isotope evidence for heterogeneous cause of oceanic anoxic events. *Nat. Commun.* **13**, 239 (2022).

98. Matsumoto, H. et al. Marine Os isotopic evidence for multiple volcanic episodes during Cretaceous Oceanic Anoxic Event 1b. *Sci. Rep.* **10**, 12601 (2020).

99. Tejada, M. L. G. et al. Ontong Java Plateau eruption as a trigger for the early Aptian oceanic anoxic event. *Geology* **37**, 855–858 (2009).

100. Bottini, C., Cohen, A. S., Erba, E., Jenkyns, H. C. & Coe, A. L. Osmium-isotope evidence for volcanism, weathering, and ocean mixing during the early Aptian OAE 1a. *Geology* **40**, 583–586 (2012).

101. Percival, L. M. E. et al. Determining the style and provenance of magmatic activity during the early Aptian oceanic anoxic event (OAE 1a). *Global Planet. Change* **200**, 103461 (2021).

102. Them, T. R. et al. Evidence for rapid weathering response to climatic warming during the Toarcian oceanic anoxic event. *Sci. Rep.* **7**, 5003 (2017).

103. Percival, L. M. E. et al. Osmium isotope evidence for two pulses of increased continental weathering linked to Early Jurassic volcanism and climate change. *Geology* **44**, 759–762 (2016).

104. Lu, X., Kendall, B., Stein, H. J. & Hannah, J. L. Temporal record of osmium concentrations and $^{187}Os/^{188}Os$ in organic-rich mudrocks: implications for the osmium geochemical cycle and the use of osmium as a paleoceanographic tracer. *Geochim. Cosmochim. Acta* **216**, 221–241 (2017).

105. Sullivan, D. L. et al. High resolution osmium data record three distinct pulses of magmatic activity during Cretaceous Oceanic Anoxic Event 2 (OAE-2). *Geochim. Cosmochim. Acta* **285**, 257–273 (2020).

106. Percival, L. M. E., van Helmond, N. A. G. M., Selby, D., Goderis, S. & Claeys, P. Complex interactions between large igneous province emplacement and global-temperature changes during the Cenomanian–Turonian oceanic anoxic event (OAE 2). *Paleoceanogr. Paleoclimatol.* **35**, e2020PA004016 (2020).

107. Jones, M. M. et al. Evaluating Late Cretaceous OAEs and the influence of marine incursions on organic carbon burial in an expansive East Asian paleo-lake. *Earth Planet. Sci. Lett.* **484**, 41–52 (2018).

108. De Lena, L. F. et al. The driving mechanisms of the carbon cycle perturbations in the late Pliensbachian (Early Jurassic). *Sci. Rep.* **9**, 18430 (2019).

109. Porter, S. J., Selby, D., Suzuki, K. & Gröcke, D. Opening of a trans-Pangaean marine corridor during the Early Jurassic: insights from osmium isotopes across the Sinemurian–Pliensbachian GSSP, Robin Hood's Bay, UK. *Palaeogeogr. Palaeoclimatol. Palaeoecol.* **375**, 50–58 (2013).

110. Porter, S. J. et al. New high resolution geochemistry of Lower Jurassic marine sections in western North America: a global positive carbon isotope excursion in the Sinemurian? *Earth Planet. Sci. Lett.* **397**, 19–31 (2014).

Acknowledgements

Author contributions

Competing interests

The authors declare no competing interests.

Additional information
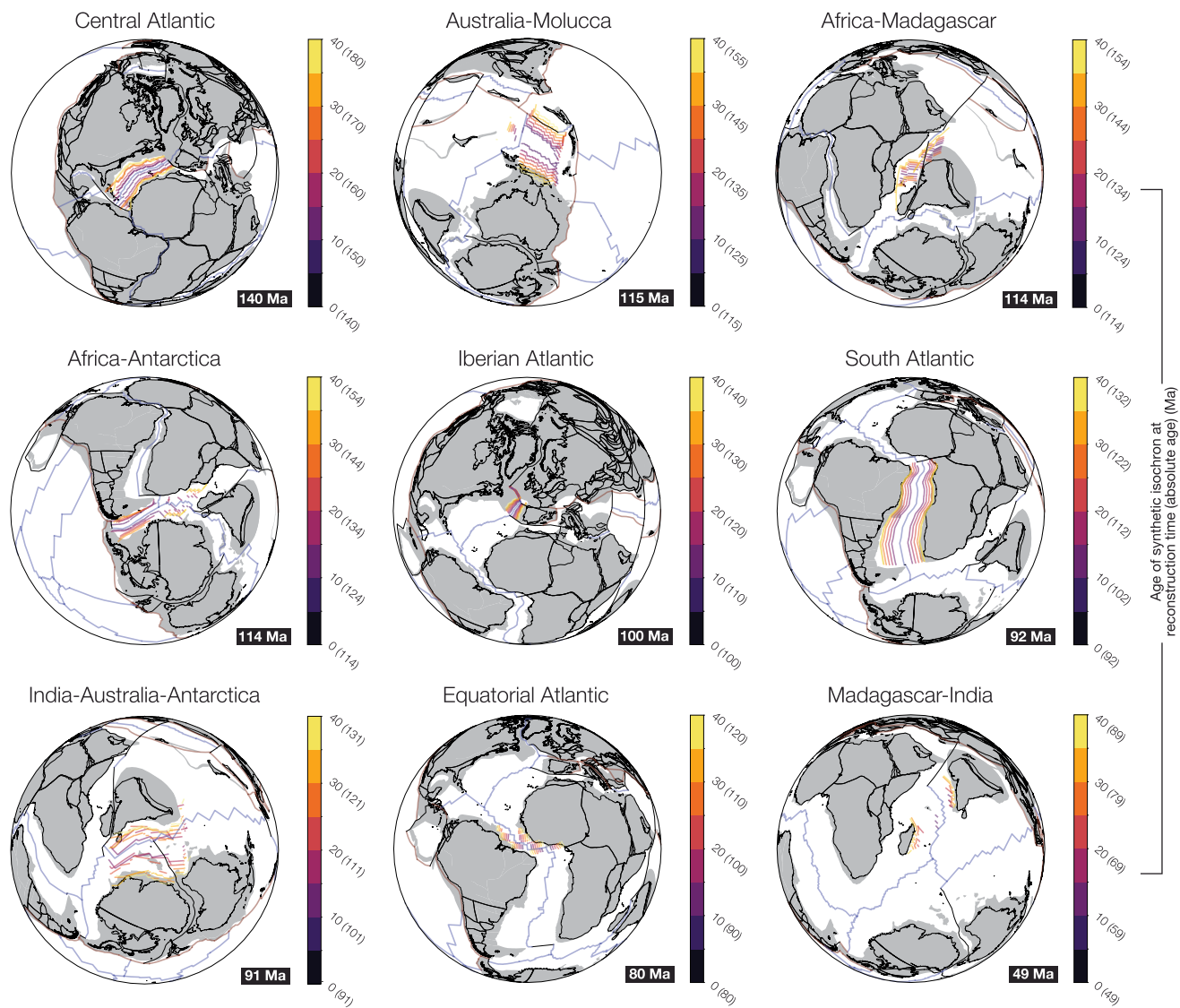
Extended data is available for this paper at https://doi.org/10.1038/s41561-024-01496-0.

Supplementary information The online version contains supplementary material available at https://doi.org/10.1038/s41561-024-01496-0.

Extended Data Fig. 1 | Spatial and temporal development of Mesozoic mid-ocean ridge systems. Plate reconstructions for the Central Atlantic, Australia-Molucca, Africa-Madagascar, Africa-Antarctica, Iberian Atlantic, South Atlantic, India-Australia-Antarctica, Equatorial Atlantic and Madagascar-India mid-ocean ridge systems, with synthetic isochrons showing the time (in Myr) relative to the reconstruction time (shown in black box); note that absolute ages in Ma are provided in brackets.
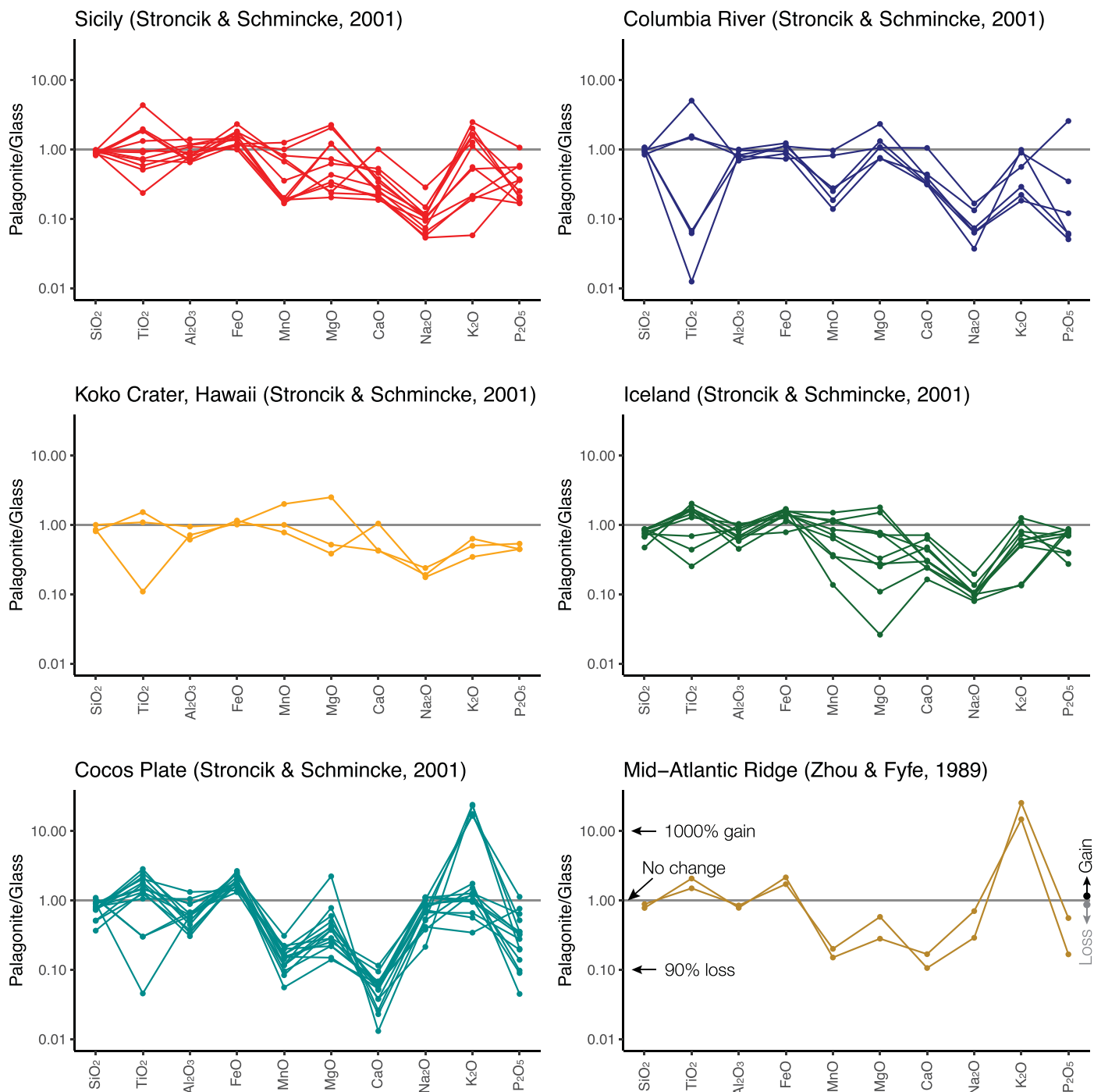
Extended Data Fig. 2 | Elemental losses sustained during basaltic glass alteration. Plots show the abundance of major elements in palagonite relative to their parental basaltic glasses. The data are from Sicily, the Columbia River, Hawaii, Iceland, and Cocos Plate[71], and the Mid-Atlantic Ridge[85]. On the plots, a value of 1 signifies no change during the glass to palagonite transition, whereas values of <1 signify a loss, and >1 a gain of the oxide. Note that a value of 0.1 corresponds to a loss of 90% of the compound (for example, as is the case for P_2O_5) as a result of palagonitization.
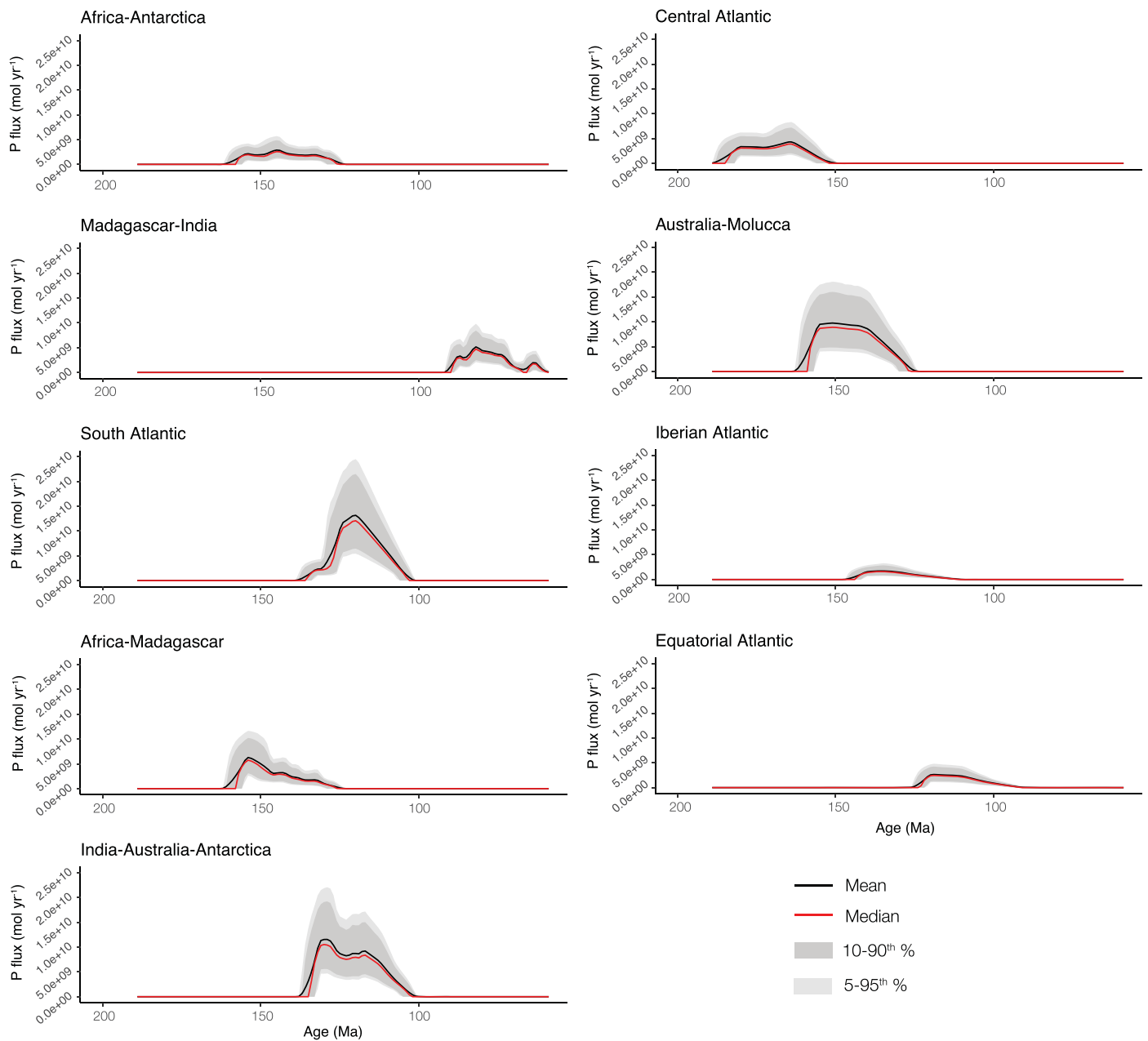
Extended Data Fig. 3 | Phosphorus output from incipient mid-ocean ridges. Modelled phosphorus release over time from the nine shallow ridge systems studied (Extended Data Fig. 1). See the Methods for further details on how the fluxes are calculated; the total flux for all ridges is shown in Fig. 3d.
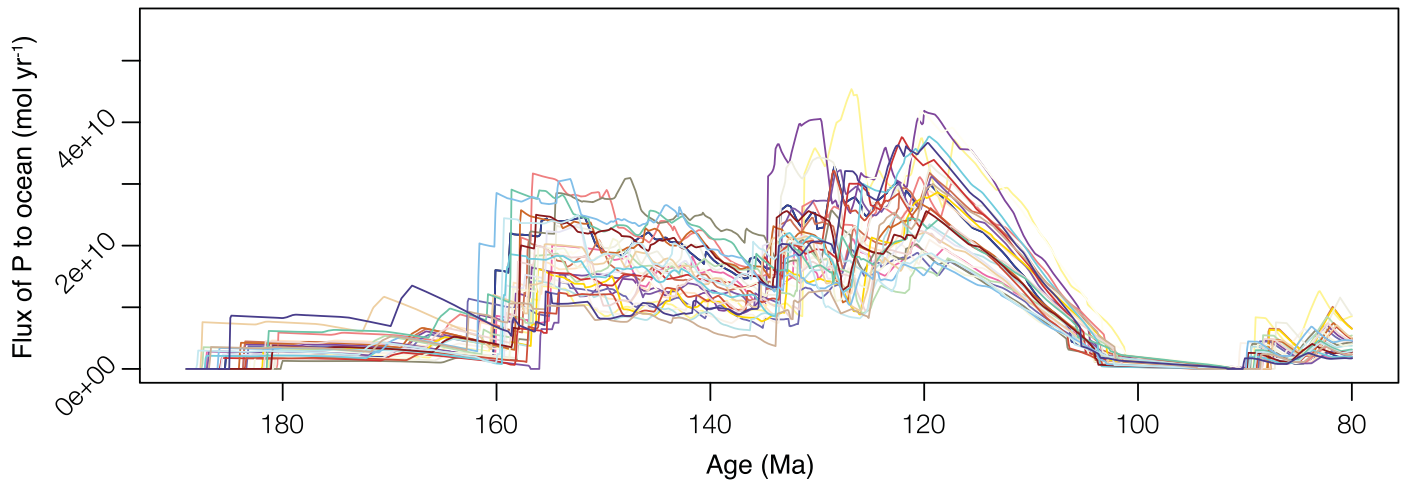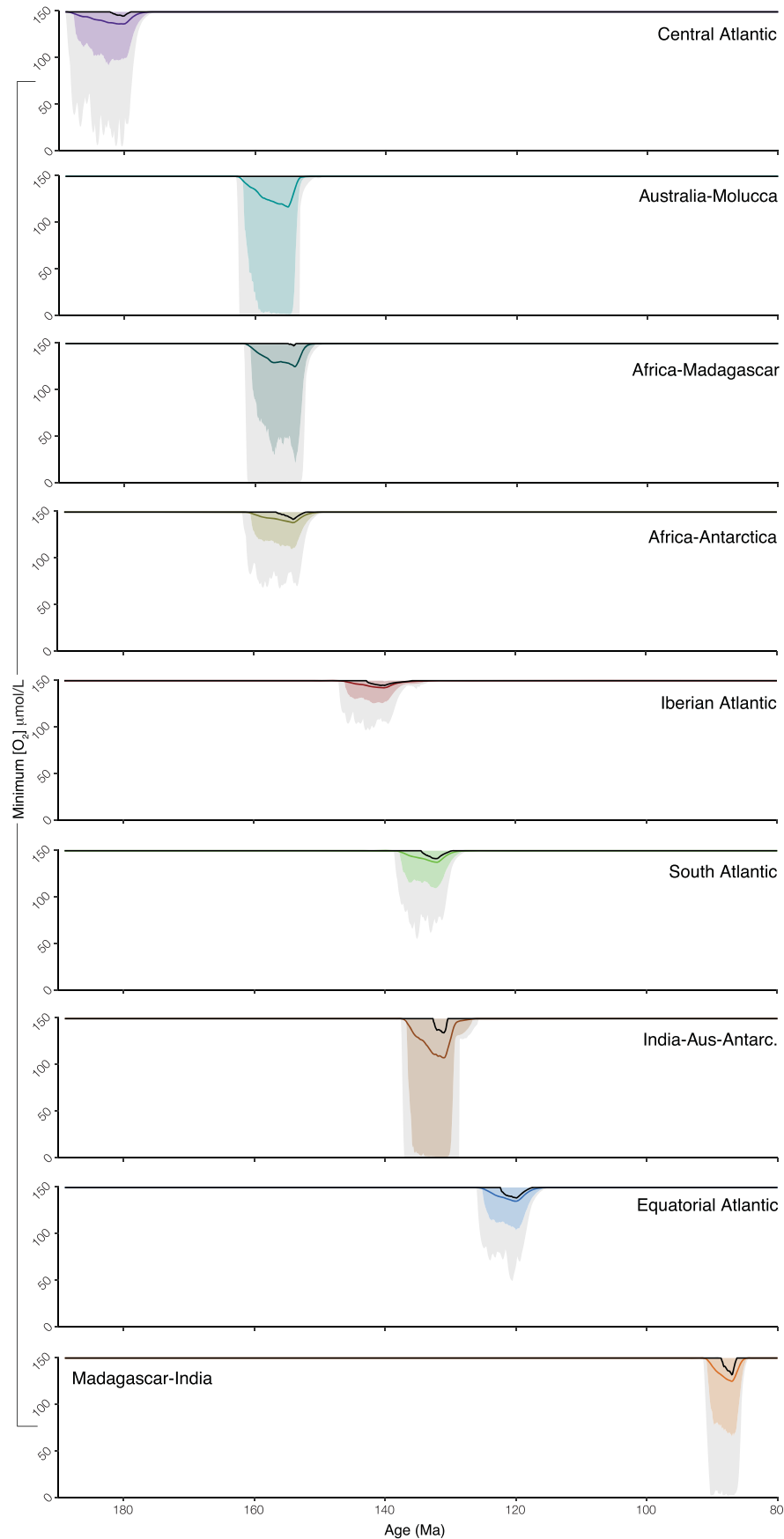
Extended Data Fig. 4 | Modelled phosphorus output from incipient mid-ocean ridges. Modelled total output of phosphorus from the nine shallow ridge systems (Extended Data Fig. 1), showing 30 individual simulations. See the Methods for further details on how the fluxes are calculated; the total flux for all ridges is shown in Fig. 3d.
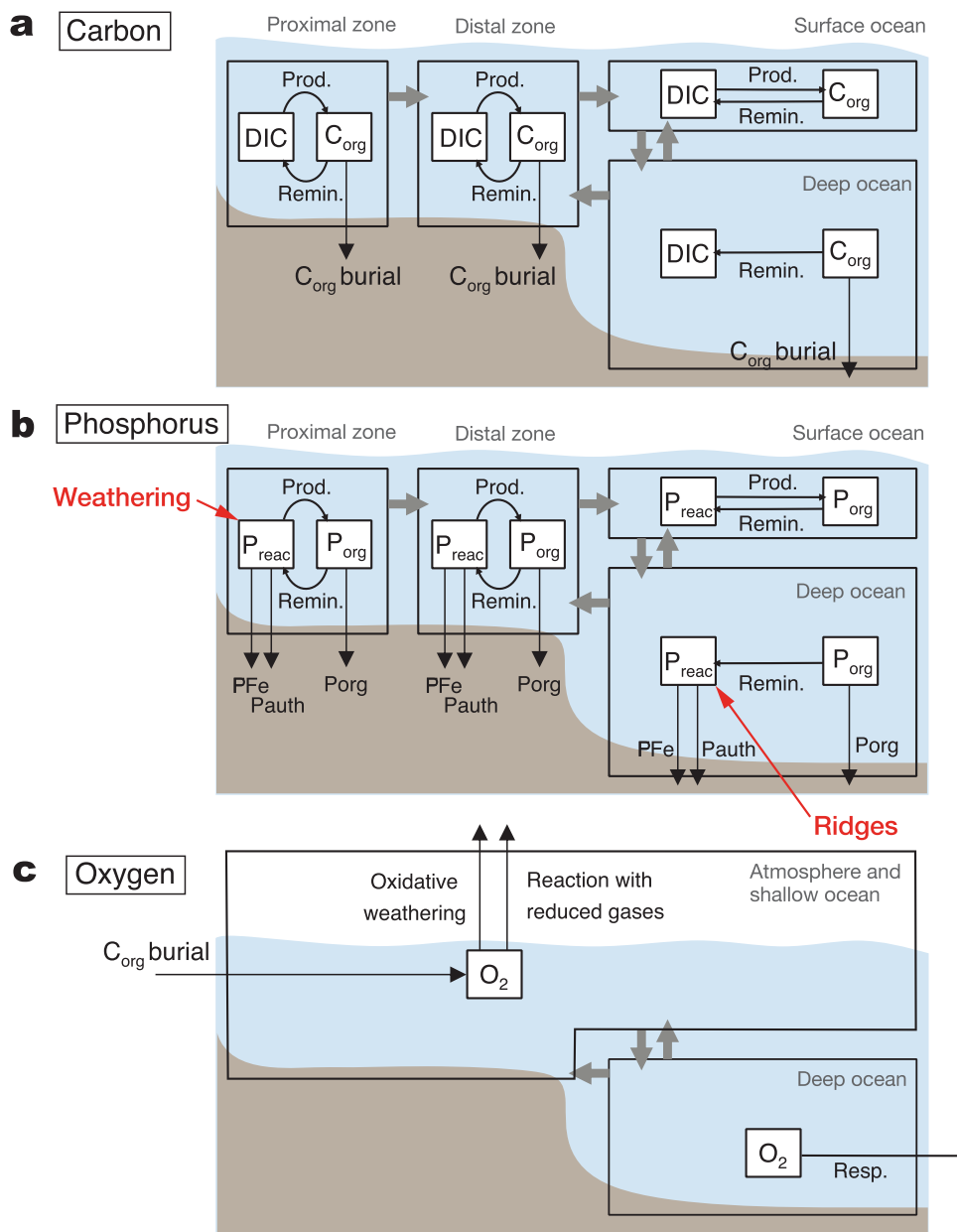
Extended Data Fig. 5 | Ocean and atmosphere box model. Clear boxes show hydrospheric reservoirs and grey arrows denote mixing between them. White boxes show chemical reservoirs and black arrows denote biogeochemical fluxes. **a**, Carbon cycle: C exists as dissolved inorganic carbon (DIC) or organic carbon (C_{org}). **b**, Phosphorus cycle: P exists as soluble reactive phosphorus (P_{reac}) and particulate organic phosphorus (P_{org}). P inputs through weathering and ridges are labelled in red. **c**, Oxygen cycle: Single oxygen reservoir encompasses all ocean boxes that exchange with the atmosphere. The reader is referred to Alcott et al.[43] for a full model description and equations.
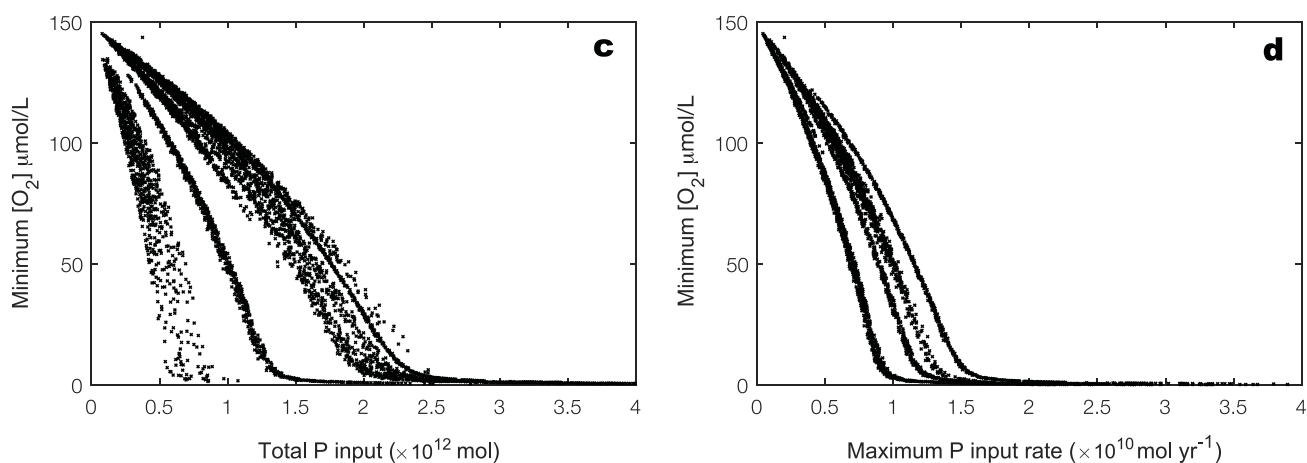
Extended Data Fig. 6 | Marine oxygen concentrations tied to ocean ridge formation. Modelled response of ocean [O₂] concentration to phosphorus output from shallow mid-ocean ridge systems (Extended Data Fig. 1). These expected ridge effects are shown individually here and combined in Fig. 5a.

Riverine inputs
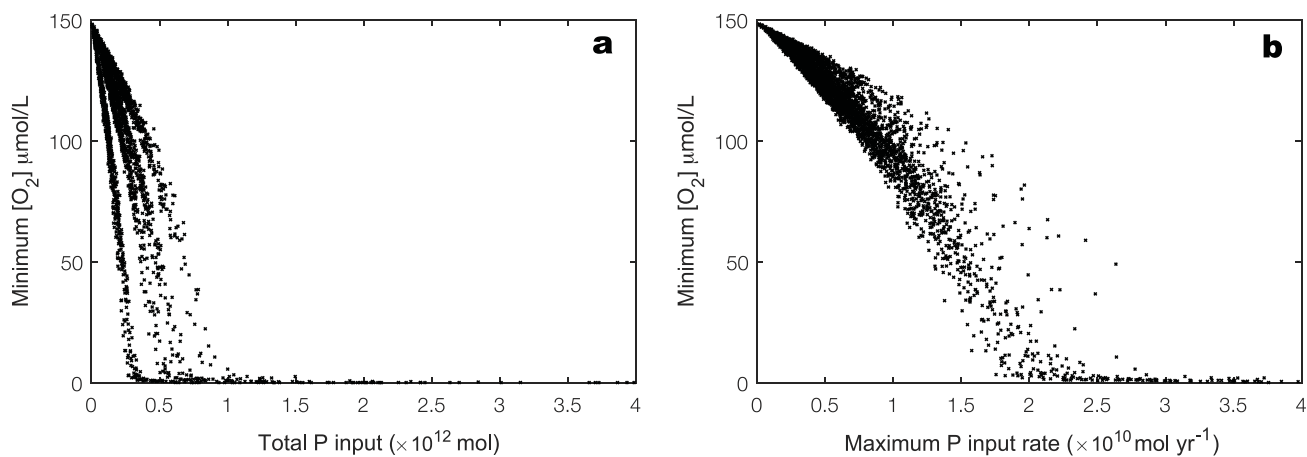
Ridge inputs

Extended Data Fig. 7 | Phase plots for subaerial and ridge phosphorus release. The upper phase plots show the effect of subaerial basalt weathering and response of (minimum) [O₂] on **a**, total P input, and **b**, maximum P input rate. The lower panels show the effect of P output, from shallow spreading ridges globally, and in particular the response of (minimum) [O₂] on **c**, total P input, and **d**, maximum P input rate. It is worth noting that although the total input of P to oceans from subaerial basalt weathering is lower, the rate of input to the oceans is at times considerably higher.
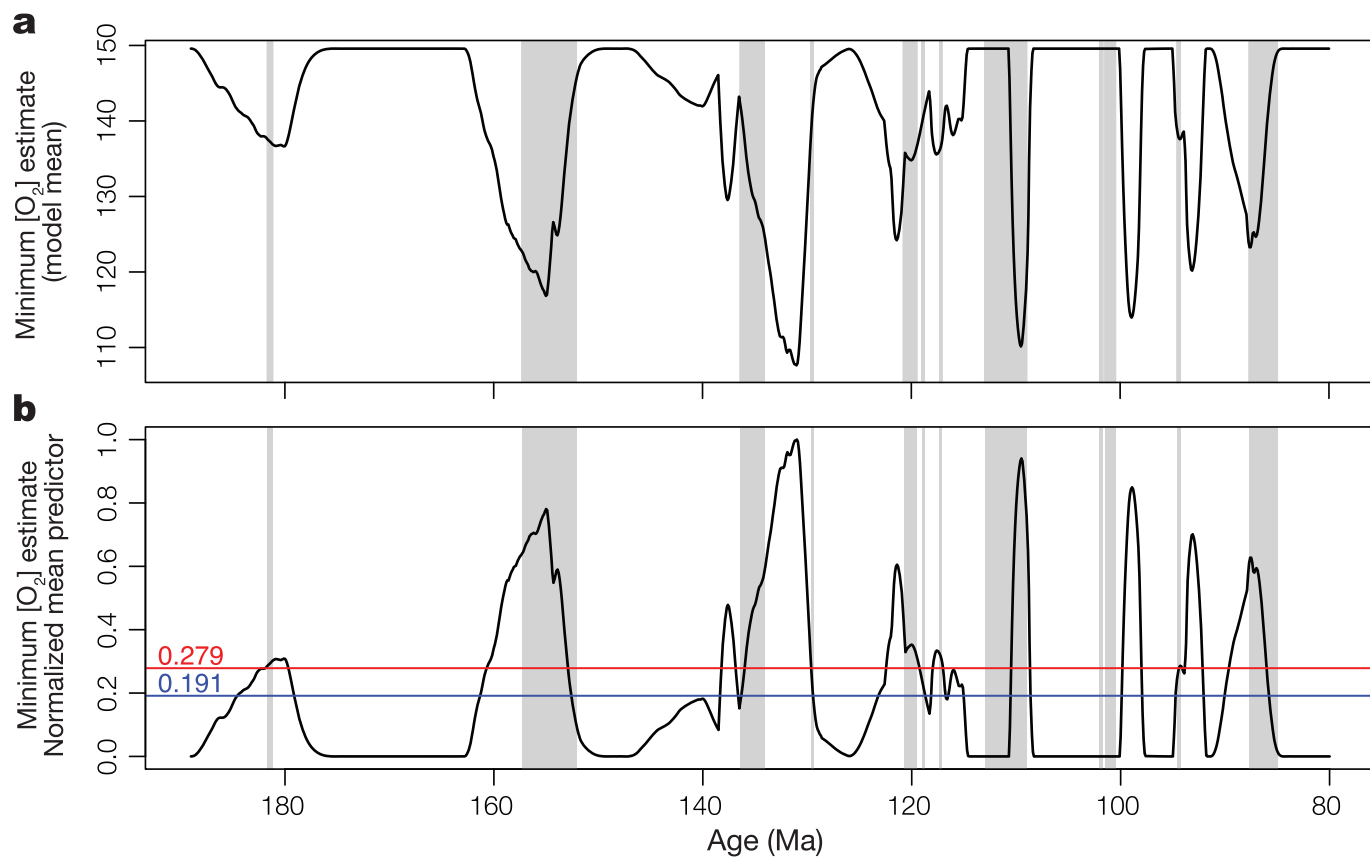
Extended Data Fig. 8 | Inputs used to the evaluate predictive performance of biogeochemical models for OAEs. a, Overall minima, using mean estimates from our biogeochemical models for ridge and weathering induced deoxygenation (Fig. 5a-b); **b**, Overall minima, normalised and inverted (1 = minimum) to apply as a predictor of OAEs (shown using vertical grey bars). The blue and red lines show two examples of potential diagnostic thresholds, using the 'Closest to top left' and Youden's statistic, respectively (see Methods; Fig. 5c).

Extended Data Table 1 | Timing and duration of Mesozoic Oceanic Anoxic Events

Age from (Ma)	Age to (Ma)	Duration (Myr)	Time interval	OAE name	Abbreviation	References
181.7†	181.2†	0.50	Early Toarcian	Toarcian OAE (Jenkyns Event)	T-OAE	ICS (2022)[87]; Jenkyns (2010)[2]
157.3†	152.1†	5.20†	Upper Jurassic	Kimmeridgian	See Note	ICS (2022)[87]; Nozaki et al. (2013)[27]
136.4	134.1	2.30	Middle Valanginian	Weissert Event	Weissert	Mattioli et al. (2014)[88]; Wouters et al. (2018)[89]
129.55	129.4	0.15	Latest Hauterivian	Faraoni Event	F-OAE	ICS (2022)[87]; Rodríguez-Tovar & Uchman (2017)[90]
126.7	*126.6*	*0.10*	*Latest Hauterivian*	*Faraoni Event*	*F-OAE*	*Matsumoto et al. (2021)[52]*
120.7	119.5	1.20	Earliest Aptian	Selli Event	OAE1a	Jenkyns (2018)[91]; Matsumoto et al. (2022)[97]
119.0	118.75	0.25	Aptian	Wezel	Wezel	Matsumoto et al. (2022)[97]
117.3	117.1	0.20	Aptian	Fallot	Fallot	Matsumoto et al. (2022)[97]
113.0	109.0	4.00	Aptian-Albian boundary	Paquier Event	OAE1b	Leckie et al. (2002)[92]; Millán et al. (2014)[93]
102.0	101.7	0.30	Late Albian	Amadeus Event	OAE1c	Leckie et al. (2002)[92]; Friedrich et al. (2018)[94]; Núñez-Useche et al. (2014)[95]
101.5	100.5	1.00	Latest Albian	Breistroffer Event	OAE1d	ICS (2022)[87]; Matsumoto et al. (2022)[97]
94.6	94.3	0.28	Cenomanian–Turonian	Bonarelli Event	OAE2	Jenkyns (2018)[91]
87.7	85.0	2.70	Coniacian-Santonian	Coniacian-Santonian	OAE3	Kouamelan et al. (2020)[96]

Table summarising the age range, duration, and time intervals of the 11 OAEs included in this study. Note that two alternative ages are provided for the Faraoni Event. Also shown for completeness is the Kimmeridgian-a protracted interval of shelf anoxia considered by some authors to represent an OAE (for example, refs. 27,86), albeit restricted to northern latitudes. Note that the timing of the Kimmeridgian event is taken as the age of that Stage as defined by the International Commission on Stratigraphy (v2022/10)[87]. The T-OAE age also uses the timing of the Pliensbachian-Toarcian boundary from ref. 88 (that is, 182.7 Ma), and it is generally thought that the T-OAE begins approximately 1 million years after the Pl-To boundary. †Note that in 2023, the Pliensbachian-Toarcian boundary was updated to 184.2 Ma, and the Kimmeridgian Stage updated to 154.8 - 149.2 Ma (that is, 5.6 Myr duration), as depicted in Fig. 4. Data from refs. 2,27,52,87–96,97.

Extended Data Table 2 | Osmium isotope data compilation

Age from (Ma)	Age to (Ma)	Data coverage (Myr)	N	Targeted OAE(s)	Reference
92.64	86.87	5.77	19	OAE3	Jones et al. (2018)[107]
94.07	92.00	2.07	27	OAE2	Percival et al. (2020)[106]
96.43	92.48	3.95	32	OAE2	Sullivan et al. (2020)[105]
111.25	93.43	17.82	73	OAE1c, OAE1d, OAE2	Matsumoto et al. (2022)[97]
121.85	110.24	11.61	124	OAE1a, Wezel, Fallot	Matsumoto et al. (2021)[28]
122.14	117.93	4.21	31	OAE1a	Bottini et al. (2012)[100]
127.53	125.53	2.00	27	F-OAE	Matsumoto et al. (2021)[52]
186.87	178.8	8.07	34	T-OAE	Them et al. (2017)[102]
183.98	180.59	3.39	25	T-OAE	Percival et al. (2016)[103]
186.62	185.93	0.69	10	NA (S–P)	De Lena et al. (2019)[108]
190.96	190.64	0.32	32	NA (S–P)	Porter et al. (2013)[109]
196.39	195.44	0.95	11	NA (S–P)	Porter et al. (2014)[110]
200.00	95.00	105.00	15	NA	Lu et al. (2017)[104]

Source of $^{187}Os/^{188}Os$ data shown in our compilation (Fig. 1e) and the time ranges covered by those data sets (note this time window does not signify OAE duration, which is shown in Extended Data Table 1). Note that ref. 28 incorporates data from refs. 98,99, and ref. 97 incorporates data from refs. 10,28,98–100,101; S-P refers to the Sinemurian-Pliensbachian stage. Data from refs. 28,52,98,102–104,105–110.